Hot stars observed by XMM-*Newton* II. A survey of Oe and Be stars[⋆]

Yaël Nazé[1],[⋆⋆] and Christian Motch[2]

[1] Groupe d'Astrophysique des Hautes Energies, STAR, Université de Liège, Quartier Agora (B5c, Institut d'Astrophysique et de Géophysique), Allée du 6 Août 19c, B-4000 Sart Tilman, Liège, Belgium
e-mail: ynaze@uliege.be

[2] Université de Strasbourg, CNRS, Observatoire Astronomique de Strasbourg, 11 rue de l'Université, F-67000 Strasbourg, France

September 11, 2018

ABSTRACT

We perform a survey of Oe and Be stars in the X-ray range. To this aim, we cross-correlated XMM-*Newton* and *Chandra* catalogs of X-ray sources with a list of Be stars, finding 84 matches in total. Of these, 51 objects had enough counts for a spectral analysis. This paper provides the derived X-ray properties (X-ray luminosities, and whenever possible, hardness ratios, plasma temperatures, and variability assessment) of this largest ever sample of Oe and Be stars. The targets display a wide range in luminosity and hardness. In particular, the significant presence of very bright and hard sources is atypical for X-ray surveys of OB stars. Several types of sources are identified. A subset of stars display the typical characteristics of O-stars, magnetic OB stars, or pre-main-sequence (PMS) objects: their Be nature does not seem to play an important role. However, another subset comprises γ Cas analogs, which are responsible for the luminous and hard detections. Our sample contains seven known γ Cas analogs, but we also identify eight new γ Cas analogs and one γ Cas candidate. This nearly doubles the sample of such stars.

Key words. stars: early-type – stars: Be – X-rays: stars – stars: individual: γ Cas

1. Introduction

Since the first sky surveys have been made in the high-energy range, it has been clear that stars of all types emit X-rays. In low-mass and young stars, this emission is directly associated with stellar activity driven by convection and hence appears linked to rotation and age (Pallavicini et al. 1981). The situation is different for massive stars, where stellar winds play a key role. These line-driven winds are indeed unstable and therefore shocks naturally occur within them, ultimately leading to soft ($kT \sim 0.2 - 0.6$ keV) and mild ($\log(L_X/L_{BOL}) \sim -7$) X-ray emission (Pallavicini et al. 1981; Berghoefer et al. 1997). Additional wind-related phenomena also occur, such as wind-wind collisions in binaries or wind magnetic confinement in magnetic objects (see Rauw & Nazé 2016; ud-Doula & Nazé 2016, for recent reviews). They lead to an increased X-ray luminosity, generally in the hard X-ray range.

In this context, O stars have generally attracted more attention than B-type stars. The reason probably is that O stars have naturally stronger winds, therefore their X-ray emission is brighter and easier to study. However, surveys and cluster observations have brought some information on B stars as well. In contrast to O stars, B stars have a lower detection rate, show large scatter in $\log(L_X/L_{BOL})$, and have hotter plasma (Berghoefer et al. 1997; Cohen et al. 1997; Nazé 2009;

Nazé et al. 2011; Rauw et al. 2015). Because of these properties and of their more tenuous winds, it has often been hypothesized that except for the earliest B stars, X-ray emission with luminosities below $L_X \sim 10^{31}$ erg s^{-1} arises from a young, solar-type, undetected companion, the intrinsic emission of the B star being negligible.

In massive stars, however, a subset of Oe and early Be stars called the γ Cas analogs were found to strongly differ from this general picture. They display a hard ($kT \sim 10$ keV) and relatively bright ($L_X = 10^{32-33}$ erg s^{-1}) X-ray emission (see Smith et al. 2016, for a recent review).

The origin of their peculiar X-rays is debated. Models have considered either a relatively low mass-accretion rate onto a compact companion or magnetic star-disk interactions. Evidence of a correlation between UV/optical and X-ray variations on short timescales (Smith & Robinson 1999; Robinson et al. 2002) as well as marked dependencies of the X-ray luminosities on decretion disk density with basically zero delay (Motch et al. 2015; Rauw et al. 2018) appear to favor the latter scenario. The γ Cas nature of π Aqr (a system with a "normal", not compact, companion near the disk, Nazé et al. 2017) further support an X-ray source located close to the Be star. It has been suggested by Motch et al. (2015) that a high stellar rotation rate close to critical plays a key role in the phenomenon, but much remains to be done to reach a full understanding of this peculiar X-ray emission.

In this paper, we perform a census of the X-ray emission of Oe-Be stars using XMM-*Newton*, *Chandra*, and *Swift* data, with two main objectives: (1) examine whether the γ Cas analog list is complete considering all currently available observations and (2) study which physical parameters are responsible for the X-ray characteristics of Oe-Be stars. Our search for γ Cas

analogs among identified Be stars is a useful complement to the search for Be stars as counterparts of X-ray sources detected in all-sky X-ray surveys (Nebot Gómez-Morán et al. 2013, 2015). The definition of the sample and the finding of counterparts are presented in Section 2, while details on data reduction appear in Section 3. The results are discussed in Section 4, and a summary concludes the paper in Section 5.

2. Sample

For this project, a list of Be stars is required first of all. Many catalogs of such stars exist, but some are too old to account for recent discoveries and their source content can be found in more recent catalogs, while others are incomplete in terms of sky coverage (they are specific to a region of the sky, e.g., Mennickent et al. 2002) or contain only candidates, with some contamination by non-Be stars (e.g., following Gkouvelis et al. 2016, only 70% of candidates in Witham et al. 2008 truly are Be stars). Although some recent papers provide a few newly discovered objects (e.g., Li et al. 2018)[1], we restricted our analysis to a single global catalog to preserve the homogeneity of our sample, and we finally decided to use the Be Star Spectra (BeSS) catalog, which is recent and "as complete as possible" (Neiner et al. 2011). It also has the additional advantage of offering optical spectra datasets of the targets, facilitating follow-up studies.

We limited ourselves to the Galaxy, because studying individual stars in the Magellanic Clouds remains a challenge even with dedicated XMM-*Newton* or *Chandra* observations (e.g., Oskinova et al. 2013; Nazé et al. 2014b). The low spatial resolution as well as the limited sensitivity of current X-ray facilities renders the identification of individual stellar sources with $L_X < 10^{32-33}$ erg s^{-1} difficult if not impossible. In addition, only "classical" Be stars were kept: very young objects (e.g., HAeBe) and Be stars belonging to high-mass X-ray binaries (HMXBs) were excluded, as their high-energy emission is of a different nature than the emission we wished to study. Finally, we had to exclude NGC 884 2079 from the list since it is a late-A star, not a Be star (Bragg & Kenyon 2002), and we merged the two entries Cl* NGC 884 LAV 1703 and [KW97] 11-2, which correspond to the same coordinates.

2.1. XMM-*Newton* serendipitous source catalog

We cross-correlated the resulting Be star list with the latest release of the XMM-*Newton* serendipitous source catalog (3XMM-DR7, see also Rosen et al. 2016) using the HEASARC archives[2]. This catalog contains 499 266 unique X-ray sources, detected in more than 9 700 EPIC observations made between 2000 February 3 and 2016 December 15. The correlation radius was set to 5", which is the point spread function (PSF) size of XMM-*Newton* and a typical value for such correlations (e.g., Antokhin et al. 2008; Claeskens et al. 2011). This led to 53 matches. The XMM-*Newton* exposures associated with these Be stars were downloaded and processed locally, leading us to discard two matches (see section 3.1 for more details). The stars and their associated 3XMM matches are presented in Table 1. This table also provides the distance between the star and its X-ray counterpart, as well as a variability flag set during the 3XMM processing. Whenever an X-ray source was bright enough, its

EPIC time series were automatically extracted and analysed by a χ^2 variability test in the processing. Sources were considered variable within the time span of the specific XMM-*Newton* exposure if the null hypothesis (constancy) was rejected with a significance level of 10^{-5} or lower. This flag was therefore only set for short-term variability in bright X-ray emitters; it does not evaluate long-term variations.

In addition, we also correlated our Be star list with the recent XMM-*Newton* archives: we searched whether any other Be star was observed in exposures that were not used for the DR7 release but are publicly available as of March 2018. Ten additional Be stars lie within the EPIC field of view of such recent XMM-*Newton* observations. We retrieved and processed these data, running a source-detection algorithm onto each of them: of the ten stars, only two (Menkhib and HD90563) are detected and were thus also added to the detection list. In total, there are thus 53 Be stars detected in XMM-*Newton* pointed observations (Table 1).

2.2. CXOGSG

The observations made by *Chandra* constitute another large set of X-ray archives. XMM-*Newton* and *Chandra* were both launched in 1999, ensuring two decades of observations. However, only the first version of the *Chandra* Source Catalog (CSC) was fully available when we began this project, and this version is limited to data that were public before the end of 2009. Therefore, we preferred to use the Chandra ACIS GSG Point-Like X-Ray Source Catalog (CXOGSG, Wang et al. 2016). It contains 217 828 distinct X-ray sources (twice more than CSCv1.1) that were found in 10 029 ACIS observations archived before 2014 December 4. As the PSF of *Chandra* is narrower than that of XMM-*Newton*, we reduced the radius to 2" for the cross-correlation with the Be star list, allowing for small astrometric errors in both X-ray and optical catalogs. This led to 31 matches, which are reported in Table 1 with the distances of their X-ray counterparts as wall as their variability flags (they were set when the source had more than ten counts and were found to be variable at a significance level of 1% in a Kolmogorov-Smirnov test).

As for XMM-*Newton*, we also correlated the Be star list with the recently archived *Chandra* exposures. Four Be stars lie in the field of view of *Chandra* observations, but only two (HD 215227 and Cl* NGC 3293 FEAS 32) were actually detected. Furthermore, one additional star that has been detected in the 3XMM-DR7, HD 42054, was observed with grating data; it is thus not included in the CXOGSG, but we downloaded and processed these observations as well. In total, there are thus 34 Be stars detected in the X-ray range by *Chandra*, 16 of which were also detected by XMM-*Newton*.

2.3. XMM-*Newton* slew survey

Finally, we cross-correlated the Be star list with the "clean" version of the second catalog of X-ray sources found in XMM-*Newton* slew data (XMMSL2, see also Saxton et al. 2008). This catalog contains 29 393 bright X-ray emitters detected in data taken between 2001 August 26 and 2014 December 31. The astrometric precision of slew data is smaller than that of pointed observations, hence the correlation radius was here enlarged to 18". We found 26 matches, half of them having been observed and detected by XMM-*Newton* or *Chandra* in pointed observations (Table 1). We requested *Swift* exposures for 6 of the re-

---

[1] For completeness, we did cross-correlate the new Oe stars that were identified in that paper with the X-ray catalogs mentioned below, but no match was found.

[2] https://heasarc.gsfc.nasa.gov/cgi-bin/W3Browse/w3browse.pl

maining sources to assess the identifications with the Be stars and secure X-ray spectra (see next sections for details).

2.4. Stellar properties

In total, 84 Be stars are associated with X-ray sources in current X-ray archives (Table 1). About two-thirds of them have usable spectra and are thus studied in more detail in Sect. 4. Table 2 lists them along with their main physical parameters, which are used throughout this paper: spectral types, magnitudes and color excesses, distances, bolometric luminosities, effective temperatures, and projected rotational velocities.

Most spectral types were extracted from the BeSS database. In the absence of a given luminosity class, we assumed a class V. Simbad provided us with V-band magnitudes, and distances were derived from Hipparcos and Gaia (DR1 and DR2) parallaxes or from photometric estimates given in the literature. In all cases, we retained the most accurate measurement. Following Luri et al. (2018), we quadratically added a $100\,\mu$arcsec systematic uncertainty to all Gaia DR2 parallaxes. Some of the brightest stars have no parallaxes in Gaia DR2 (Gaia Collaboration et al. 2018) or have parallaxes that appear to be less accurate than those provided by DR1 or by the new Hipparcos reduction of van Leeuwen (2007).

The vast majority of the E(B-V) excesses were extracted from the Stilism database[3] (Capitanio et al. 2017) using the distance estimates. For the most distant targets that are located beyond the limit of the Stilism database, we used the infrared 3D map of Marshall et al. (2006) or took values from the literature. We assumed Av = 3.1×E(B-V).

To derive bolometric luminosities, we used the bolometric corrections from Nieva (2013), $\log(T_{eff})$ given by de Jager & Nieuwenhuijzen (1987) and absolute V magnitudes from Wegner (2007). For binaries, this implies that the bolometric luminosities correspond to the pair, not to the Oe-Be star alone. Moreover, the quoted errors on bolometric luminosities only reflect distance uncertainties. In general, our photometric bolometric luminosities match those expected for the stellar spectral types quite well (using the calibration of de Jager & Nieuwenhuijzen 1987, e.g.). In addition, projected rotational velocities were extracted from various catalogs queried in Vizier; references are provided in the table footnote.

Finally, flags are provided in the last column of the table to indicate if a star is a known (close) binary, pulsating star, γ Cas analog (Smith et al. 2016), or magnetic object (Grunhut et al. 2017; Schöller et al. 2017). Regarding the latter characteristics, a comment must be made. Magnetic fields are not detected in "true" Be stars (Grunhut et al. 2012) and theoretical models indeed demonstrate that the presence of a disk is incompatible with the strong dipolar fields detectable in spectropolarimetric surveys (ud-Doula et al. 2018). However, magnetic stars may display emission lines, hence some of them may have been classified as "Be" in the past and appear in the BeSS. We thus kept these few cases as a comparison point (for more details on the high-energy emission of magnetic massive stars, see Nazé et al. 2014a).

3. Data reduction

3.1. XMM-*Newton*

We downloaded from the archives all XMM-*Newton* datasets associated with the Be stars detected in the 3XMM. In addition, we downloaded the recent datasets that are not included in the 3XMM DR7, with the Be stars Menkhib, HD 55135, CD−44 4392, HD 90599 and HD 90563, HD 305627, HD 306111, HD 117172, V807 Cen, and HD 225985 in their fields of view. These XMM-*Newton* data were locally processed with the Science Analysis Software (SAS) v16.0.0 using calibration files available in Oct. 2017 and following the recommendations of the XMM-*Newton* team[4].

These observations were taken in various mode and filter combinations. We checked in each case that the filter was adapted to the target optical/UV luminosity. This was the case for all but three stars: (1) all observations of 48 Lib were taken with a thin filter, while the target magnitude requires a thick filter and the X-ray data therefore suffer from heavy optical loading and cannot be used (this target was thus discarded from the list of matches reported in Table 1); (2) One observation of V374 Car (ObsID=0113891201, Rev.164) was taken with a medium filter rather than a thick one like the other exposures and this dataset was therefore discarded from further analyses; (3) The observations of V807 Cen were taken with the thin filter rather than the medium one but since the star is not detected (see below), this does not change the analyses. We also checked modes, as they allow for different levels of pile-up. Considering the 3XMM count rates, three potential problems exist: (1) from its count rates, π Aqr is at the limit of pile-up, but a previous, dedicated study showed that there is no pile-up problem for the XMM-*Newton* data (Nazé et al. 2017); (2) BZ Cru is much too bright in X-rays for the full-frame mode used in ObsIDs 0109480101/201/401, hence those datasets were discarded; (3) γ Cas was observed in small-window mode, but its EPIC count rates still are above the pile-up limits, although a run of *epatplot* does not reveal the typical signatures of pile-up and we therefore kept the circular extraction as in Smith et al. (2012b).

After the initial pipeline processing, the European Photon Imaging Camera (EPIC) observations were filtered to keep only the best-quality data (PATTERN 0–12 for MOS and 0–4 for pn). To assess the crowding near the targets in order to choose the best extraction region, a source detection was performed on each EPIC dataset using the task *edetect_chain*, which uses first sliding box algorithms and then performs a PSF fitting, on the 0.3–10.0 keV energy band and for a log-likelihood of 10. In this context, we note that, regarding the recent datasets, only Menkhib and HD 90563 are detected, and they were thus added to the detection list (Table 1). Furthermore, the results on the older datasets indicated no formal detection for NGC 869 1164, HD 93190, BQ Cru, or HD 228860: these sources thus are faint, at the limit of detection (indeed, the DR7 processing considers a log-likelihood detection level of 6, which is lower than our local processing). Except for HD 93190, which was clearly detected by *Chandra* as well, some doubt may thus be cast on the detection of the other three stars. In particular, it should be noted that BQ Cru is also detected to be extended in the 3XMM catalog, unlike all other matches that are considered as point-like sources. In this context, doubts may also arise when considering the case of HD 305891, as the source appears to lie within

---

Table 1. List of Be stars detected in the X-ray range, ordered by RA.

#	Star name	3XMM	d(")	var.?	XMM-*Newton* ObsID	CXOGSG	d(")	var.?	*Chandra* ObsID	XMMSL2	d(")	*Swift* ObsID
1	γ Cas	J005642.4+604300	0.0	y	0651670201/301/401/501,0743600101					J005642.6+604301	1.0	
2	Achernar	J013742.7-571413	1.7	n	0402120101							
3	V782 Cas	J020845.6+650215	1.5	n	0102580801							
4	Cl* NGC 869 LAV 1039					J021908.5+570348	1.2	y	5407,9912/3,12021			
5	NGC 869 1164:	J021914.1+571105	3.4		0201160201							
6	HD 14162					J021927.5+570817	0.7	n	5407,9912/3,12021			
7	Cl* NGC 884 LAV 1703:	J022125.1+571148	4.7		0201160301							
8	HD 17505									J025107.7+602503	1.9	
9	HD 19818									J030827.0-592231	9.4	00010532001/2
10	Merope					J034619.5+235653	0.3	n	13,366,17250/1/2			
11	Menkhib	none	1.3		0770990101/201					J035858.0+354729	2.5	
12	λ Eri	J050908.8-084514	0.6	n	0402120301							
13	25 Ori	J052444.8+015047	0.5	n	0554610101	J052444.8+015047	0.1		8571			
14	V1230 Ori	J053520.8-052144	1.0	n	0212480301,0403200101	J053520.7-052144	0.2	y	*c*			
15	43 Ori	J053522.8-052457	0.7	n	0212480301,0403200101	J053522.8-052457	0.5	y	*c*			
16	HD 42054	J060703.6-341843	0.0	y	0402121401	none			11021,12226			
17	PZ Gem	J062715.8+145321	0.5		0670080301,0760220601							
18	Cl* NGC 2244 PS 26					J063129.7+045449	0.4	n	1874,3750			
19	Cl* NGC 2244 JOHN 33					J063215.4+045520	0.3	y	1874,3750			
20	15 Mon	J064058.6+095345	0.7	n	0011420101	J064058.6+095344	0.2	n	5401,6247/8	J064058.2+095348	6.6	
21	19 Mon	J070254.7-041421	0.3		0761090901							
22	HD 57682	J072202.1-085845	0.8	n	0650320201							
23	BN Gem	J073705.7+165415	0.3		0670080201							
24	V392 Pup	J074610.5-375601	0.2	n	0694730301/401							
25	V374 Car	J075850.5-604928	0.2	n	0113890601/1001/1101, 0126511201,0134531201/301/501	J075850.5-604928	0.1	n	65/6,1229,1232,1458			
26	HD 90563	none	2.3		0780070701							
27	Cl* NGC 3293 FEAS 32					none	0.3		16648			
28	HD 93190	J104419.5-591700	1.8		0109530101/201/301/401	J104419.5-591659	0.3	y	9484			
29	HD 93843					J104837.7-601325	0.2	n	9508,9857			
30	HD 305891:	J110230.1-604854	2.0	y	0111210201,0152570101							
31	Phecda									J115350.6+534143	6.1	
32	V863 Cen	J120805.2-503941	0.5	n	0742340101							
33	δ Cen	J120821.5-504320	0.4	n	0742340101							
34	BZ Cru	J124250.3-630331	0.1	y	0504730101					J124250.7-630328	2.9	
35	BQ Cru:	J124332.8-630607	4.5		0109480101/201/401							
36	HD 117357	J133115.1-614357	2.8		0720300201							
37	HD 119682	J134632.5-625524	0.2	y	0087940201,0551000201	J134632.5-625523	0.2	n	8929,10834/5/6	J134631.8-625529	7.7	
38	μ Cen:	J134936.7-422822	3.5	n	0402121701							
39	V767 Cen	J135357.1-470741	1.2	y	0402121801					J135357.1-470739	2.5	
40	CQ Cir									J145050.6-601659	5.6	00042457001/2, 00042464001, 00010536001
41	V1040 Sco					J155355.8-235841	0.4	n	13624			
42	δ Sco	J160019.9-223718	0.4	n	0743660101							
43	ζ Oph					J163709.5-103401	0.4	n	2571,4367	J163709.4-103402	1.3	
44	HD 153295					J170025.2-421900	0.1		8234,8237			
45	V1075 Sco	J171519.2-333254	0.1	n	0554440101					J171518.7-333251	7.8	
46	γ Ara	J172523.7-562239	0.6	n	0201550101					J172523.8-562240	0.7	
47	V750 Ara	J172754.7-470134	0.5	y	0551020101					J172754.3-470132	5.7	
48	α Ara									J173150.8-495233	2.8	
49	V864 Ara									J173311.8-583324	5.2	

Table 1. Continued.

#	Star name	3XMM	d(")	var.?	XMM-*Newton* ObsID	CXOGSG	d(")	var.?	*Chandra* ObsID	XMMSL2	d(")	*Swift* ObsID
50	Cl* NGC 6383 FJL 24	J173448.0-323520	0.8	n	0001730201							
51	V3892 Sgr	J174445.7-271344	0.7	y	0201200101,0691760101	J174445.7-271344	0.2	n	8647	J174445.6-271351	6.9	
52	HD 316341					J174835.5-295729	0.1	y	8743			
53	V771 Sgr									J175328.3-244630	2.3	00043742001/2002/9002, 00010533001/2
54	HD 316568	J175442.6-294346	0.9	n	0206590201,0402280101	J175442.7-294347	0.9	n	4547,5303			
55	ALS 4570:					J180223.0-230158	1.9	y	2566			
56	Cl* NGC 6530 ZCW 175	J180411.1-242145	0.6	n	0008820101,0720540401/501/601	J180411.1-242145	0.3	y	977,3754,4397,4444			
57	HD 164906	J180425.8-242309	1.1	n	0008820101,0720540401/501/601	J180425.8-242308	0.1	n	977			
58	Cl* NGC 6530 ZCW 221	J180429.3-242527	3.2	n	0008820101,0720540401/501/601	J180428.9-242525	0.6	n	977			
59	Cl* NGC 6530 ZCW 228	J180432.9-241844	0.4	n	0008820101,0720540401/501/601	J180432.9-241844	0.2	n	977,3754,4397,4444			
60	V4379 Sgr									J180533.3-194514	0.9	00010535001
61	HD 165783	J180827.1-195207	1.1		0152833001,0672320201							
62	Cl* NGC 6611 PPM 38					J181839.7-134656	0.2		978			
63	BD-13 4928	J181842.8-134649	1.7		0605130101	J181842.7-134650	0.2	y	978			
64	Cl* NGC 6611 BKP 29783:	J181846.1-135438	3.2	n	0605130101							
65	BD-13 4933					J181904.8-134820	0.4	n	978,8932,9864/5,9872			
66	EM* AS 315	J184059.9-052749	2.6		0604820301							
67	CX Dra									J184643.3+525916	2.2	
68	HD 344783					J194306.7+231612	0.3	n	10502,10517			
69	HD 190864	J200539.7+353628	0.2	n	0556260301							
70	HD 228438	J201350.1+363721	1.4		0720600101							
71	HD 228860:	J201851.5+365740	0.5		0510011401,0552350101							
72	V2188 Cyg					J203318.5+411535	0.2		4511,109556/7/8			
73	W Del	J203740.0+181703	0.4		0742500601							
74	HD 198931	J205209.7+442604	0.5	n	0679580201							
75	V2156 Cyg									J212501.9+442707	3.1	00010534001/2/3
76	Alfirk	J212839.5+703338	0.1	n	0300490201/301/401/501					J212839.7+703339	0.8	
77	ε Cap									J213704.0-192755	12.1	
78	EM Cep					J215348.1+623651	0.2	n	8938,10818/19/20			
79	π Aqr	J222516.6+012238	0.2	y	0720390701					J222517.0+012226	14.4	
80	HD 215227	J224257.2+444315	3.2		0723610201	none	0.9		16753			
81	EM* MWC 659									J224743.4+571652	17.0	00010537001
82	BD+61 2355:	J225229.0+624112	3.5		0743980301							
83	V810 Cas					J232019.0+554828	0.1	n	3453			
84	β Scl									J233258.5-374906	3.3	

Notes. : A colon indicates a dubious identification (see section 3 for details) ; [c]=3,4,18,1522,2567/8,3498,3744,4373/4,4395/6,4473/4,7407/8/9/10/11/12,8568,8589,8895/6/7,13637,14334/5,15546,17735. ALS 4570 is used for the BeSS entry HD164492D since the two objects have the same coordinates. In case of multiple observations (hence multiple detections of a star under the same X-ray source name), the closest separation is provided.

Table 2. Physical properties of the targets.

#	Object	Spectral type[a]	V band	E(B-V)[b]	distance (pc)	Origin of distance[c]	$\log(L_{\mathrm{BOL}}/L_\odot)$	$\log(T_{eff})$[d]	$v_{rot}\sin i$[e] (km s^{-1})	Flags
1	γ Cas	B0IVpe	2.39	0.044	190 ± 20	DR1	4.73± 0.09	4.486	295 [17]	γ
2	Achernar	B6Vpe	0.46	0.001	43 ± 1	DR1	3.42± 0.02	4.138	218 [18,19]	
3	V782 Cas	B2.5III:[n]e+[s]	7.62	0.483	955 ± 96	DR2	4.15± 0.09	4.284	188 [20,21]	
4	Cl* NGC 869 LAV 1039	B3e	12.37	0.609	2293 ± 85	[10]	3.20± 0.03	4.297		
5	NGC 869 1164	A0e	14.72	0.630	2293 ± 85	[10]	1.63± 0.03	3.991		
6	HD 14162	Be	9.29	0.642	2549 ± 680	DR2	4.92± 0.24	4.477		
7	Cl* NGC 884 LAV 1703	B2IVe	12.24	0.662	2346 ± 87	[10]	3.43± 0.03	4.339		
8	HD 17505	O6.5III((f))n+O8V [s]	7.07	0.763	3032 ± 886	DR2	6.36± 0.26	4.596	126 [22]	+
9	HD 19818	B9.5Vne	9.06	0.017	309 ± 10	DR2	1.47± 0.03	4.023		
10	Merope	B6IVe	4.18	0.021	106 ± 5	DR2	2.80± 0.04	4.166	229 [17,18,19]	
11	Menkhib	O7.5IIIe	4.06	0.201	397 ± 78	DR1	5.03± 0.17	4.553	230 [23]	+
12	λ Eri	B2IVne	4.27	0.021	249 ± 11	DR1	3.87± 0.04	4.339	295 [18,19]	
13	25 Ori	B1Vpe	4.96	0.026	260 ± 25	DR2	3.78± 0.08	4.405	278 [17,18,19]	
14	V1230 Ori	B8IVve	9.74	0.038	436 ± 22	DR2	1.66± 0.04	4.088		
15	43 Ori	O9.5Vpe	6.39	0.052	459 ± 61	DR2	3.95± 0.12	4.508	133 [23]	+
16	HD 42054	B4IVe	5.84	0.010	337 ± 15	DR2	3.31± 0.04	4.252	220 [18]	
17	PZ Gem	O9pe	6.64	0.139	834 ± 76	DR2	4.54± 0.08	4.536	265 [18,19]	γ
18	Cl* NGC 2244 PS 26	B7Ve	11.41	0.266	759 ± 83	[11]	1.77± 0.10	4.096		
19	Cl* NGC 2244 JOHN 33	B6Vne	12.01	0.382	1390 ± 100	[12]	2.29± 0.06	4.138		
20	15 Mon	B1Ve	4.64	0.011	288 ± 41	DR1	3.97± 0.12	4.405	55 [19,23]	+,m?
21	19 Mon	B1Ve	5.00	0.032	376 ± 31	H07	4.09± 0.07	4.405	272 [17,18,24]	*
22	HD 57682	O9Ve	6.43	0.143	1266 ± 177	DR2	4.99± 0.12	4.536	16 [25]	m
23	BN Gem	O8Vpev	6.87	0.031	650 ± 176	DR1	4.11± 0.24	4.554	247 [18,19]	
24	V392 Pup	B7Ve	5.87	0.010	204 ± 6	DR2	2.53± 0.03	4.096		
25	V374 Car	B2IVnpe	5.81	0.088	325 ± 26	H07	3.57± 0.07	4.339	224 [18]	
26	HD 90563	B2Ve	9.86	0.685 [1]	3743 ± 1277	DR2	4.72± 0.31	4.320		
27	Cl* NGC 3293 FEAS 32	B8Ve	12.87	0.290 [2]	2750 ± 250	[2]	2.25± 0.08	4.058		
28	HD 93190	O9.5e	8.84	1.500 [3]	3276 ± 1024	DR2	6.42± 0.28	4.500		
29	HD 93843	O6IIIe	7.33	0.250 [4]	2846 ± 791	DR2	5.53± 0.25	4.578		m?
30	HD 305891	B3Ve	10.37	1.500 [3]	2737 ± 767	DR2	3.74± 0.25	4.274		
31	Phecda	A0Ve+K2V	2.44	0.001	26 ± 1	H07	1.86± 0.02	3.991	168 [26,27,28]	+
32	V863 Cen	B6IIIe	4.47	0.009	102 ± 3	DR2	2.58± 0.03	4.140	111 [18]	m
33	δ Cen	B2Vne	2.52	0.011	128 ± 8	H07	3.94± 0.05	4.320	228 [18,19]	
34	BZ Cru	B0.5IVpe	5.31	0.331	421 ± 28	DR2	4.55± 0.06	4.455	338 [18,19]	γ
35	BQ Cru	Be	12.05	0.950 [5]	2600 ± 80	[5]	3.08± 0.03			
36	HD 117357	O9.5Ve	9.58	0.365	1605 ± 615	DR1	4.09± 0.35	4.508	78 [18]	*
37	HD 119682	B0Ve	7.90	0.332	1752 ± 325	DR2	4.86± 0.16	4.512	200 [19]	γ
38	μ Cen	B2Vnpe	3.43	0.013	155 ± 4	H07	3.75± 0.02	4.320	150 [18,19]	
39	V767 Cen	B2Ve	6.10	0.070	830 ± 100	[13]	4.20± 0.11	4.320	100 [19]	
40	CQ Cir	B1Ve	10.04	0.462	1803 ± 333	DR2	3.96± 0.16	4.405	335 [19]	
41	V1040 Sco	B2Ve	5.40	0.110 [6]	141 ± 4	DR2	3.00± 0.02	4.320	312 [17,18,19]	m
42	δ Sco	B0.2IVe	2.32	0.142	154 ± 21	H07	4.69± 0.12	4.486	165 [17]	+
43	ζ Oph	O9Ve	2.56	0.203	113 ± 3	H07	4.51± 0.02	4.536	335 [18,19,23]	m?
44	HD 153295	B2e	9.10	0.559	1684 ± 322	DR2	4.17± 0.17	4.300		
45	V1075 Sco	O8Ve	5.53	0.269	1022 ± 167	DR2	5.35± 0.14	4.554	81 [18,25]	m?
46	γ Ara	B1IIe	3.34	0.100	343 ± 19	H07	4.63± 0.05	4.343	281 [29]	
47	V750 Ara	B2Vne	6.66	0.142	1124 ± 152	DR2	4.33± 0.12	4.320	277 [18]	γ
48	α Ara	B2Vne	2.95	0.006	83 ± 6	H07	3.38± 0.06	4.320	279 [18,30]	
49	V864 Ara	B7Vnnpe	7.03	0.058	242 ± 6	DR2	2.27± 0.02	4.096		
50	Cl* NGC 6383 FJL 24	B9Ve	11.38	0.460	1518 ± 266	DR2	2.46± 0.15	4.023		
51	V3892 Sgr	Oe	9.13	0.783	1233 ± 175	DR2	4.68± 0.12	4.536	260 [18]	γ
52	HD 316341	B0Ve	9.88	0.773	2022 ± 466	DR2	4.65± 0.20	4.477	120 [19]	
53	V771 Sgr	B3/5ne [s]	9.16	0.311	780 ± 97	DR2	3.45± 0.11	4.428		
54	HD 316568	B2IVpe	9.66	0.540 [3]	2328 ± 597	DR2	4.27± 0.23	4.339		
55	ALS 4570		6.80	1.630	2950 ± 450	[14]	7.48± 0.13	4.564	33 [23]	
56	Cl* NGC 6530 ZCW 175	B3Ve	10.37	0.388	1074 ± 131	DR2	3.01± 0.11	4.274		
57	HD 164906	B0Ve	7.38	0.431	1260 ± 177	DR2	4.83± 0.12	4.477	255 [19]	
58	Cl* NGC 6530 ZCW 221	B2.5Ve	10.70	0.350	1329 ± 191	DR2	3.07± 0.13	4.297		
59	Cl* NGC 6530 ZCW 228	B2.5Vne	10.45	0.375	1076 ± 131	DR2	3.02± 0.11	4.297		
60	V4379 Sgr	B9Ve	7.05	0.070	122 ± 45	DR2	1.46± 0.33	4.023		
61	HD 165783	B4IIe	8.37	0.634	1593 ± 278	DR2	4.24± 0.15	4.176		
62	Cl* NGC 6611 PPM 38	B8Ve	13.71	0.893	1750 ± 50	[15]	2.27± 0.02	4.058		
63	BD-13 4928	O9.5Vne	10.04	0.330 [7]	2220 ± 210	[7]	4.21± 0.08	4.508		
64	Cl* NGC 6611 BKP 29783	Be	13.59	0.963	1750 ± 50	[15]	3.30± 0.02	4.477		
65	BD-13 4933	B0.5Ve	10.63	1.100	2264 ± 631	DR2	4.77± 0.25	4.443		

Table 2. Continued

#	Object	Spectral type[a]	V band	E(B-V)[b]	distance (pc)	Origin of distance[c]	$\log(L_{BOL}/L_\odot)$	$\log(T_{eff})$[d]	$v_{rot}\sin i$[e] (km s^{-1})	Flags
66	EM* AS 315	Be	11.30	1.310 [3]	4653 ± 1979	DR2	5.41± 0.39	4.477		
67	CX Dra	B2.5Ve	5.90	0.024	357 ± 15	DR2	3.45± 0.04	4.297	159 [17,19,30]	+
68	HD 344783	B0IVe	9.80	0.604	1785 ± 857	DR2	4.30± 0.45	4.486		
69	HD 190864	O7IIIe	7.78	0.600	2143 ± 458	DR2	5.51± 0.19	4.562	55 [23,25]	
70	HD 228438	B0.5IIIe	8.37	0.660	2702 ± 716	DR2	5.26± 0.24	4.429	219 [18]	
71	HD 228860	B0.5IVe	9.72	1.070	2083 ± 440	DR2	5.07± 0.19	4.455		
72	V2188 Cyg	B2Ve*	14.88	2.570 [8]	1500 ± 200	[16]	4.34± 0.12	4.339		
73	W Del	A0Ve	9.81	0.050	820 ± 73	DR2	1.98± 0.08	3.991		+
74	HD 198931	B1Vnne	8.72	0.407	825 ± 172	DR2	3.74± 0.18	4.405	322 [18]	
75	V2156 Cyg	B1.5Vnnpe	8.91	0.312	943 ± 94	DR2	3.59± 0.09	4.364		
76	Alfirk	B2IIIev	3.23	0.007	105 ± 11	DR2	3.44± 0.09	4.305	26 [17,25]	+
77	ε Cap	B3Vpe	4.55	0.006	155 ± 17	DR2	3.19± 0.09	4.274	237 [17,19,30]	
78	EM Cep	B0.5Ve	7.03	0.210	530 ± 141	H07	3.85± 0.24	4.443		
79	π Aqr	B1Ve	4.64	0.059	241 ± 16	H07	3.88± 0.06	4.405	243 [17,18,19]	+,γ
80	HD 215227	B5ne	8.81	0.250 [9]	2575 ± 654	DR2	4.05± 0.23	4.200	262 [18]	
81	EM* MWC 659	B0IIIpe	10.15	0.420	4290 ± 1632	DR2	4.69± 0.35	4.465		
82	BD+61 2355	B7IVe	9.63	0.268	576 ± 50	DR2	2.30± 0.08	4.125		
83	V810 Cas	B1npe	8.59	0.288	1625 ± 271	DR2	4.24± 0.15	4.405	422 [18]	
84	β Scl	B9.5IVmnpe	4.37	0.001	54 ± 1	H07	1.86± 0.01	4.053	26 [28]	

Notes. [a] All spectral types are from the BeSS database except for those marked with [s], which are from Simbad. In this context, we note that Simbad mentions O7V, F5III, and B0.5III as spectral types for the companions of 15 Mon, CX Dra, and Alfirk, respectively. [b] all E(B-V) extracted from the Stilism interface at http://stilism.obspm.fr (Capitanio et al. 2017) unless specified otherwise. [c] DR1; Gaia DR1 (Gaia Collaboration et al. 2016), DR2: (Gaia Collaboration et al. 2018), H07: (van Leeuwen 2007) [d] after de Jager & Nieuwenhuijzen (1987). [e] Mean of values from all quoted references.
Flags: An asterisk indicates a pulsating object; a cross identifies binaries; [γ] is set for known γ Cas analogs, and [m] indicates magnetic stars ([m?] is for claimed magnetic objects). We note that Alfirk's primary is a pulsating magnetic star, while the secondary is of Be type; the temperature and rotational velocity values provided here are those of the secondary.
References: [1] Kaltcheva & Golev (2012). [2] Baume et al. (2003). [3] E(B-V) from (Marshall et al. 2006). [4] Wegner (1993). [5] Piatti & Clariá (2001). [6] Gontcharov & Mosenkov (2018). [7] Selim et al. (2016). [8] Wright et al. (2010). [9] this paper. [10] Currie et al. (2010). [11] Sung et al. (1997). [12] Hensberge et al. (2000). [13] Schöller et al. (2017). [14] Savage et al. (1985). [15] Guarcello et al. (2007). [16] Maryeva et al. (2017). [17] Abt et al. (2002). [18] Yudin (2001). [19] Zorec et al. (2016). [20] Głębocki & Gnaciński (2005) [21] Jaschek & Egret (1982) [22] Uesugi & Fukuda (1970). [23] Simón-Díaz & Herrero (2014). [24] Huang et al. (2010). [25] Simón-Díaz et al. (2017). [26] Evans (1967). [27] David & Hillenbrand (2015). [28] Royer et al. (2007). [29] Ochsenbein & Halbwachs (1987). [30] Chauville et al. (2001).

extended emission, although the 3XMM detection officially has zero extension.

Before we extracted the spectra, light curves for events beyond 10 keV were calculated for the full cameras, and when background flares were detected, the corresponding time intervals were discarded. In some cases, the light curves indicated continuous flaring during the observation, and such exposures were discarded to avoid problems or strong noise in data. Other exposures of the same target usually existed, hence no information was lost. There is one exception, however: only one exposure exists for V782 Cas, and it is contaminated by strong flares. To check whether this caused any problem, we extracted the spectra of two other sources that were also situated at large off-axis angles in this (sparsely populated) field of view. One is brighter and one fainter than V782 Cas. These spectra are all different, as could be expected if background is well corrected, hence the spectrum of V782 Cas can be trusted.

We extracted EPIC spectra using the task *especget* in circular regions centered on the Simbad positions of the targets and with radii between 12.5 and 30″, depending on the crowding. Only for V1230 Ori, 43 Ori, and V750 Ara were elliptical regions used as the sources are far off-axis and their PSF is strongly distorted. Background was derived in nearby circular regions devoid of sources. Dedicated ancillary response file (ARF) and redistribution matrix file (RMF) response matrices, which are used to calibrate the flux and energy axes, respectively, were also calculated by this task. EPIC spectra were grouped with *specgroup* to obtain an oversampling factor of five and to ensure that a minimum signal-to-noise ratio of 3 (i.e., a minimum of ten counts) was reached in each spectral bin of the background-corrected spectra; unreliable bins below 0.25 keV were discarded.

Reflection grating spectrometer (RGS) data were also processed using the initial pipeline, but only for sources that are bright and centered in the field of view: γ Cas, V1075 Sco, δ Sco, Alfirk, and Menkhib. As for EPIC data, a flare filtering was also applied (using a threshold of 0.12 cts s^{-1}) when needed. Dedicated response files were calculated for both orders and both RGS instruments, and were subsequently attached to the source spectra for analysis. These high-resolution data are not reported here in detail, but they were used to check the results of the EPIC spectral fits.

Finally, it is also important to examine the distance between the detected DR7 counterpart and the Be star. Most (80%) of the X-ray counterparts appear within 2″ of the optical position of the star, including in the case of the new detections, but there are a few exceptions with separations of 3–5″: NGC 869 1164 (3XMM J021914.1+571105 at 3.4″), Cl* NGC 884 LAV 1703 (3XMM J022125.1+571148 at 4.7″), BQ Cru (3XMM J124332.8-630607 at 4.5″), μ Cen (3XMM J134936.7-422822 at 3.5″), Cl* NGC 6530 ZCW 221 (3XMM J180429.3-242527 at 3.2″), HD 215227 (3XMM J224257.2+444315 at 3.2″), Cl* NGC 6611 BKP 29783 (3XMM J181846.1-135438 at 3.2″), and BD+61 2355 (3XMM J225229.0+624112 at 3.5″). We examined each case in turn. First, we just registered doubts

about X-rays associated with BQ Cru, and this decentering only added to the problem. To investigate the issue for other sources, we then examined the distance between other X-ray sources detected in the field of view and their known optical counterparts. For μ Cen, only the high proper motion star UCAC3 96-143035 seems to be detected in addition to μ Cen, but its 3XMM counterpart, 3XMM J134901.2-422841, lies at 0.7" of the optical source. For BD+61 2355, the field of view is centered on 2MASS J22535512+6243368, which is at 0.2" from its counterpart 3XMM J225355.1+624336, and other sources seem well centered (e.g., 2MASS J22531578+6235262, which is at a similar off-axis angle as BD+61 2355, is at 0.4" of its counterpart 3XMM J225315.8+623526). In the field of Cl* NGC 884 LAV 1703, the late-A star NGC 884 2079 lies at 0.5" of 3XMM J022142.9+571830. This seems to indicate the absence of astrometric problems in these datasets, hence the association of these three Be stars with the 3XMM sources are doubtful. Finally, *Chandra* data also exist for the remaining sources, and help settle the association question. For Cl* NGC 6530 ZCW 221, there is an X-ray source at the position of the star, but it is very close to a brighter source, and this neighbor may have led to some confusion in the XMM-*Newton* data, explaining the decentering. For HD 215227, the *Chandra* data clearly indicate an X-ray source at 0.8" of the position of the star, so there is no doubt about the association. Conversely, the *Chandra* data covering the positions of NGC 869 1164 and Cl* NGC 6611 BKP 29783 reveal no source at the positions of the stars, but sources nearby, which may have led to an incorrect match in the XMM-*Newton* data. For example, NGC 869 1171 is twice closer to 3XMM J021914.1+571105 than NGC 869 1164 and corresponds to an X-ray source in *Chandra* data. All dubious identifications are clearly marked by a colon in Table 1. In this context, it is also interesting to mention the case of Cl* NGC 6530 SCB 790-HD 164947[5], which is at 2-2.6" of 3XMM J180441.6-242056. The field is crowded, and in the *Chandra* data, it is clear that the emitter is a neighboring source (CXOGSG J180441.6-242055 lies at 2" of HD 164947). We therefore discarded it from the list of matches. As a last step, the separation between X-ray and optical sources also needed to be compared to the uncertainty on the X-ray position. For the vast majority of the sources, both the separations and the errors are smaller than 2". The separation is smaller than three times the positional error for all sources except for 15 Mon (for which the error is small because of its X-ray brightness, but the separation is only 0.7") and Cl* NGC 884 LAV 1703 (as discussed above; the separation nearly reaches 5" in this case).

3.2. Chandra

We downloaded from the archives all *Chandra* datasets associated with the Be stars detected in the CXOGSG. In addition, we downloaded the grating data associated with HD 42054 as well as recent datasets, not included in the CXOGSG, with the Be stars V402 Car, CW Cep, Cl* NGC 3293 FEAS 32, and HD 215227 in their field of view. These *Chandra* data were locally reprocessed with CIAO 4.9 and CALDB 4.7.3.

A source detection using wavelets (*wavdetect*) was run on these new datasets, considering the full energy band, PSF maps, and two scale sizes. Only Cl* NGC 3293 FEAS 32 and HD 215227 are detected, providing for the latter a confirmation of the XMM-*Newton* detection.

[5] There are two separate entries in the BeSS for these stars, but Cl* NGC 6530 SCB 790 is really HD 164947A.

Regarding CXOGSG counterparts, we may note that most matches occur within 1", including for the new detections. Only Cl* NGC 869 LAV 1039 and ALS 4570 show larger distances (1.2 and 1.9", respectively) from their CXOGSG counterpart. In the latter case, this separation reaches nearly twice the minimum positional error (set to 1" in CXOGSG), which makes this optical-X-ray match clearly an outlier compared to others. The associated data reveal that ALS 4570 appears at a moderate off-axis angle. Its PSF is elongated, but this is also the case of neighboring sources such as HD164492B, which lies at 0.1" of its CXOGSG counterpart, CXOGSG J180223.6-230145, or V2282 Sgr, which is at 0.4" of CXOGSG J180216.7-230346, hence the Be counterpart identification may be somewhat doubtful.

ACIS spectra were then extracted using the task *specextract*, which also calculated the adequate *weighted* response matrices. Unweighted ARF and RMF matrices provide very similar results, although often with slightly higher fluxes, in all cases except for V374 Car. Source regions were generally circles of 2.5" radii centered on the Simbad positions of the sources, while the surrounding annuli, with radii 2.5" and 7.5", were used for background extraction. In some cases, however, the source region had to be elliptical rather than circular because of the PSF distorsion far off-axis; in other cases, depending on crowding, nearby circles also replaced the annuli for background definition. In addition, for bright sources, an annular source extraction was also performed to be able to check for pile-up. In case of grating data, zeroth-order spectra of the targets were always extracted. Moreover, if the target was observed on-axis and was X-ray bright (HD 119682, HD 42054, ζ Oph, and 15 Mon), spectra from orders +1 and –1 were combined using *combine_grating_spectra* to obtain the final HEG and MEG spectra. As for RGS, those high-resolution data are not reported here, but they were used to check the spectral fits. All *Chandra* spectra were grouped in the same way as the XMM-*Newton* spectra.

Finally, it is important to note that we detected some pile-up in the ACIS-I, low-resolution spectra of 43 Ori (most ObsID), 15 Mon (ObsID 2550), HD 119682 (ObsID 4554), and ζ Oph (ObsID 14540). These spectra clearly appear harder than the available, non piled-up XMM-*Newton* spectra, the zeroth-order spectra of the same targets in other *Chandra* observations, or spectra corresponding to annular extraction regions. They were therefore discarded. Only the zeroth-order *Chandra* spectra that were not affected were thus kept for these stars.

3.3. Swift

For a subset of stars detected in the XMM slew survey (Table 1), XRT data from the Neil Gehrels *Swift* Observatory were requested. All but V4379 Sgr are optically faint targets ($V > 8.5$) and can therefore be observed with the XRT in PC mode. To avoid optical loading, the WT mode was used instead for V4379 Sgr. The other XMMSL2 sources are too optically bright for the PC mode but also too X-ray faint for the WT mode and therefore cannot be observed by *Swift*. Data were processed locally using the XRT pipeline of HEASOFT v6.22.1 with calibrations v20170501. For V771 Sgr, snapshots with ObsIDs 00043749001, 00043749003, and 00043749004 were discarded because very few counts were recorded for the source and/or a high background is present.

The source spectra were extracted within Xselect using circular regions of 20 px (47.1″) radius. The surrounding annuli (with radii 20-60 px, or 47.1-141.4″) were used for background for all but a few cases in which the source lies too close to
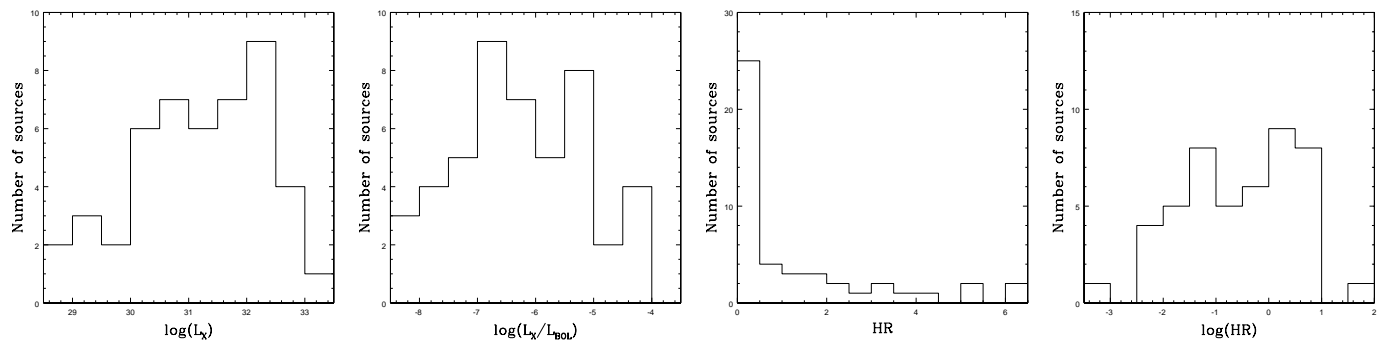
Fig. 1. Histograms of the X-ray luminosities, X-ray to bolometric luminosity ratios, and hardness ratios. When several observations of the same object existed, the values used to derive the histograms correspond to averages. The dubious cases (colons in Table 1) are not considered in these figures and that the high-luminosity parameters of PZ Gem were used.

the field-of-view edge; in these cases, a nearby circle devoid of sources was considered instead. The RMF matrix from the calibration database was used, but specific ARF response matrices were calculated for each dataset using *xrtmkarf*, considering the associated exposure map. Because of their small number of counts, we combined the spectra of the same source taken in different *Swift* exposures using the ғтооᴌs *addpha* and *addarf*. The weights for ARF combinations were in proportion to the number of counts collected in the individual spectra. Combinations of individual spectra were also provided by the online tool[6]. Their fitting formally yields slightly higher fluxes than the fitting of our locally processed and combined data, but the results remain similar within errors; the results provided below correspond to a simultaneous fitting of the online and local combined spectra. The spectra were binned using *grppha* in a similar manner as the XMM-*Newton* spectra.

4. Results

4.1. Derivation of X-ray properties

4.1.1. Spectral fits

We examined each individual spectrum and fit it only if there were enough counts (or bins) to do so, which was the case for 51 stars. Table 3 provides the fitting results. Fitting was made within Xspec v12.9.1p using absorbed optically thin thermal plasma models typical of massive stars X-ray emission (i.e., *tbabs* × *phabs*×$\sum$ *apec*), with solar abundances of Asplund et al. (2009). In these models, the first absorption component represents the interstellar column, which was fixed to the value derived from the known color excess using the formula of Gudennavar et al. (2012, $N_{\mathrm{H}}^{ISM} = 6.12 \times 10^{21} \times E(B−V)\,\mathrm{cm}^{-2}$). The second absorption allows for possible additional (local) absorption, for example, due to the stellar winds or the decretion disks. For the emission components, we used up to three temperatures: we added thermal components only if a single component did not provide a satisfactory fit. For XMM-*Newton* data, all available EPIC spectra were fit simultaneously.

For the few sources in common, we checked our results with those reported in the Chandra Carina complex project (Nazé et al. 2011), in the X-ray survey of magnetic stars (Nazé et al. 2014a), and in γ Cas analog papers (Lopes de Oliveira et al. 2007, 2010). A good agreement was found (considering that slightly different distances and/or interstellar extinctions were sometimes used in those studies).

For the brightest (and a few faintest) objects in the sample, the reduced χ^2 of the best fits are sometimes larger than two, which rendered these fits formally inacceptable. These results were kept, however, notably because even in these cases, the fitting was good in the 0.5–10.0 keV energy band where the flux was estimated (some deviations may occur in 0.2–0.5 keV). The problems mostly come from the impact of nonsolar abundances and/or unrealistically small error bars in the case of very bright sources (that do not account for the calibration systematics). For γ Cas objects, larger χ^2 may also occur because their fluorescence Fe line is not fit (this choice was made to keep the spectral fitting homogeneous among all targets, and it did not affect the values of global fluxes or hardness ratios examined in this paper). In some cases, one spectral parameter (usually absorption) was fixed because unrealistic errors yielded erratic results that prevented us from deriving correct errors on the other parameters and on the fluxes. Finally, we calculated the X-ray luminosities, using the X-ray fluxes corrected for interstellar absorptions and the known distances (Table 2). The log(L_X/L_{BOL}) ratios further take into account the derived bolometric luminosities (see Section 2.4). Hardness ratios were calculated as the ratios between the interstellar medium (ISM) corrected fluxes in the hard (2.0–10.0 keV) and soft (0.5–2.0 keV) energy bands.

4.1.2. Simple detections

When there were not enough counts for a meaningful spectral analysis, we derived the source X-ray luminosities, corrected for interstellar absorption, from the count rates. The XMM-*Newton* catalogs provide such count rates in 0.2–12 keV (band 8) for MOS1, MOS2, and pn in the case of the XMM-DR7 and for pn only in the case of the XMM-SL2. The optical blocking filter that was used (thin, medium, or thick) is known for the DR7 cases, but not for the slew survey: for this survey, we considered both thin and thick filters to obtain extreme values. In one case, the detection is new (HD 90563), so that the count rates of each instrument were estimated by a local run of the detection routine. For *Swift*, we derived the count rate in the 0.3–10 keV energy band from a run of the online tool[7]. For *Chandra*, the CXOGSG catalog does not provide count rates; however, fluxes are available for most of the detections in the CSC (v1.1 or v2, although the latter is incomplete at the time of writing). These fluxes do not rely on any model, they simply correspond to the sum of the energies of each incident source photon, scaled by the local value of the ARF at the location of the incident photon.

We converted these count rates or observed photon fluxes using WebPIMMS[8] for absorbed apec models, as suitable for massive stars. In these models, the absorbing column was fixed to the interstellar one (estimated using the color excess of Table 2 and the formula of Gudennavar et al. 2012). Furthermore, since the actual spectral properties are unknown and a range of temperatures was found for the thermal components in the spectral fits (see previous section), we decided to convert count rates for two temperatures in order to obtain upper and lower limits: values of 0.3 keV and 15. keV were chosen as they were typically found as extremes in our spectral fits. Table 4 provides the resulting ranges in X-ray luminosities (corrected for interstellar absorption) with the associated $\log(L_X/L_{BOL})$ values.

4.2. Discussion

While dedicated studies of a few Oe or Be stars exist, no large survey has been performed up to now. Only smaller studies have been published, with mixed results. Meurs et al. (1992) reported the detection of ten Oe-Be stars in the *ROSAT all-sky-survey*. They found similar luminosities but a slightly lower detection rate for Oe-Be stars compared to OB stars. Also using *ROSAT*, Cohen et al. (1997) in contrast reported a higher detection rate for Be stars than for B stars (all with types B1.5 or later). They also derived similar distributions in $\log(L_X/L_{BOL})$ for both categories, although with a higher median value for their seven Be stars. These previous works possess two drawbacks: small statistics (only seven to ten stars in their samples) and a low-energy range (because of the use of *ROSAT*). Fortunately, this can now be easily corrected with the current generation of X-ray facilities, although the lack of all-sky surveys prohibits deriving global detection rates.

Figure 1 provides the histograms of the X-ray properties derived from our spectral fits (47 sources after discarding potentially dubious cases). Our targets cover a wide range of X-ray luminosities and $\log(L_X/L_{BOL})$ ratios, larger than in general surveys of OB stars, but similar to what is seen for magnetic objects (see Fig. 2 of Nazé et al. 2014a). The presence of a second peak at $\log(L_X/L_{BOL}) \sim -5.5.. -5$ is unprecedented, however: in surveys, only few objects display such high ratios. In parallel, half of the stars display hardness ratios below 0.5: they are thus relatively soft sources as is usual for OB stars, magnetic or not (see the right panels of Fig. 8 of Nazé et al. 2014a). Again, there is a significant difference, however: our Be sample clearly displays a substantial fraction of much higher hardness values, which is not typical for OB stars.

More detailed plots (Fig. 2) show a general trend between hardness and brightness, that is, the brightest sources (both in terms of L_X and $\log(L_X/L_{BOL})$) always display a harder emission. The associated correlation coefficient is not very high, however: it reaches 69% when considering $\log(L_X/L_{BOL})$ and $\log(HR)$, and only 19% when considering L_X and HR. It may also be interesting to note that Fig. 2 does not show a clear-cut separation between stars or groups of stars. In particular, while the known γ Cas analogs appear mixed with a few objects presenting the same properties (see Section 4.2.2 below), the whole category (known cases + new detections) does not appear to be fully isolated from the other sources of the sample.

4.2.1. Oe and Be that are not γ Cas analogs

Fig. 2 (for spectral fit cases) and Table 4 (for HD 117357) show that Oe stars display a soft emission with the typical $\log(L_X/L_{BOL})$ of O-stars ($\log(L_X/L_{BOL}) \sim -7$). The only exceptions are γ Cas analogs (see next subsection), BD–13°4928, and the known binary 43 Ori. In the latter case, colliding wind emission, magnetic activity, and/or contamination by companions have been discussed in the literature as possibly affecting its X-ray emission (see Schulz et al. 2006; Gagné et al. 2008). In particular, small-amplitude and short-term flares were attributed to a pre-main-sequence (PMS) neighbor (Gagné et al. 2008), but we detect in our dataset a much larger variation in X-ray luminosity than reported before. In a *Chandra* exposure (ObsID 4474), 43 Ori brightens by one order of magnitude, reaching γ Cas characteristics (see below). However, some pile-up may artificially harden the spectrum in this case, therefore we do not count it as a secure γ Cas candidate. A more thorough investigation with more observations clearly needs to be performed to understand the nature of the X-ray emission of this system. Up to now, BD–13°4928 was unknown to display a particularly bright X-ray emission. However, with only a slightly harder character than common O-stars, it certainly does not show a rather flat spectrum at high energies, typical of the very hot plasma detected in γ Cas objects. The most likely candidates for explaining its X-ray properties are thus colliding winds or magnetic confinement, hence this target should be monitored, both optically and in X-rays.

Magnetic objects display a wide spread in X-ray luminosities, wider than for the Oe stars in our sample and γ Cas objects. However, they remain less hard and less luminous than the latter ones, and their properties are in line with those reported in an X-ray survey of magnetic stars (Nazé et al. 2014a).

PMS companions of massive stars are difficult to detect in the optical range, therefore it is possible that some of our Oe and Be targets possess such a companion. This is not without consequence on the X-ray properties. PMS stars can indeed reach 10^{31} erg s^{-1} when flaring, and they also appear to be harder ($kT \sim 1 - 2$ keV) than typical O-stars at the time. The top panels of Fig. 2 show that the latest stars in our sample, that is, those with the lowest bolometric luminosities ($\log(L_{BOL}/L_\odot) < 2$), have $L_X \sim 10^{31}$ erg s^{-1} and moderate hardness ratios, reflecting such confusion with a nearby active star. The situation appears more mixed for $\log(L_{BOL}/L_\odot) = 2$ to 4, as lower X-ray luminosities and hardness ratios also exist. The large scatter observed in this region suggests that it contains both contamination and true emission from the Be stars.

4.2.2. γ Cas analogs: new detections

One of our objectives was to determine whether the census of γ Cas analogs in current data was complete. Before we address this point, the characteristics of such stars must be recalled. γ Cas analogs were essentially defined on the basis of the X-ray and optical properties of the two brightest objects, namely, γ Cas itself and BZ Cru. The overall characteristics of these two stars and of other γ Cas analogs are summarized in Smith et al. (2016). Their most outstanding X-ray feature is the presence of a strong thermal component with kT ≥ 5-6 keV (although lower temperature components also exist, but with a lower intensity), yielding a broad band X-ray luminosity of $\sim 10^{32-33}$ erg s^{-1}. The X-ray luminosity is thus intermediate between that of "normal" OB stars and of HMXBs.

---

[8] https://heasarc.gsfc.nasa.gov/cgi-bin/Tools/w3pimms/w3pimms.pl
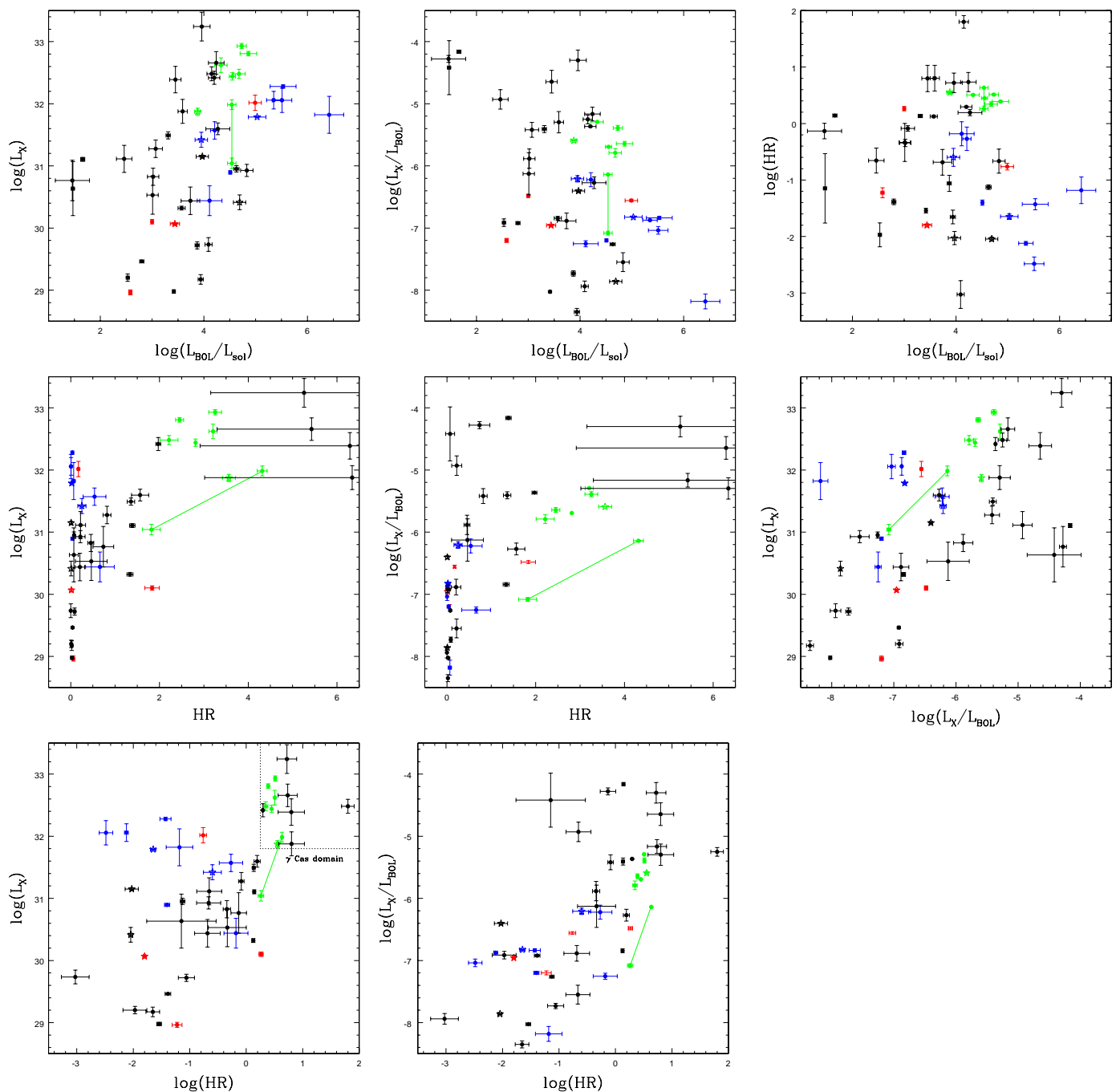
Fig. 2. Comparisons of X-ray luminosities, bolometric luminosities, X-ray to bolometric luminosity ratios, and hardness ratios, taken by pairs. Green, red, blue, and black symbols correspond to known γ Cas objects, known magnetic objects (including Alfirk because of its magnetic secondary), non-γ Cas and non-magnetic O-type stars, and all other stars, respectively. Stars are used for known binaries (see Table 2), simple dots otherwise. As in Fig. 1, dubious cases are not shown and averages are used in case of multiple observations, the errors corresponding to the scatters around the means. For PZ Gem, both low-flux and high-flux cases are shown, as they differ significantly; they are connected so they can be easily spotted.

Our analyses confirm the properties of the known γ Cas analogs and further provide additional criteria that may constitute interesting alternatives or complements to existing criteria. The hardness ratio, defined as the ratio between the hard (2.0–10.0 keV) and soft (0.5–2.0 keV) ISM-corrected fluxes, is usually easy to compute with a few counts and is an excellent proxy for temperature: Table 3 shows that $HR > 1.6$ correspond to kT ≥ 5 keV. In addition, the log(L_X/L_{BOL}) ratio is also high for γ Cas analogs, usually reaching at least –6, a value that is extreme even

for magnetic or colliding-wind O stars. Finally, Fig. 3 shows that γ Cas analogs are also remarkable in terms of hard X-ray luminosity, with $L_X(hard) \geq 10^{31}$ erg s^{-1}. It may be noted that such boundaries exclude the possible contributions of even the most extreme PMS companion stars.

All previously known γ Cas analogs dwell well inside this parameter region. However, they are not alone: these criteria enable us to discover eight new analogs (Table 5, Fig. 7). Spectra are available for seven of them (Fig. 4):
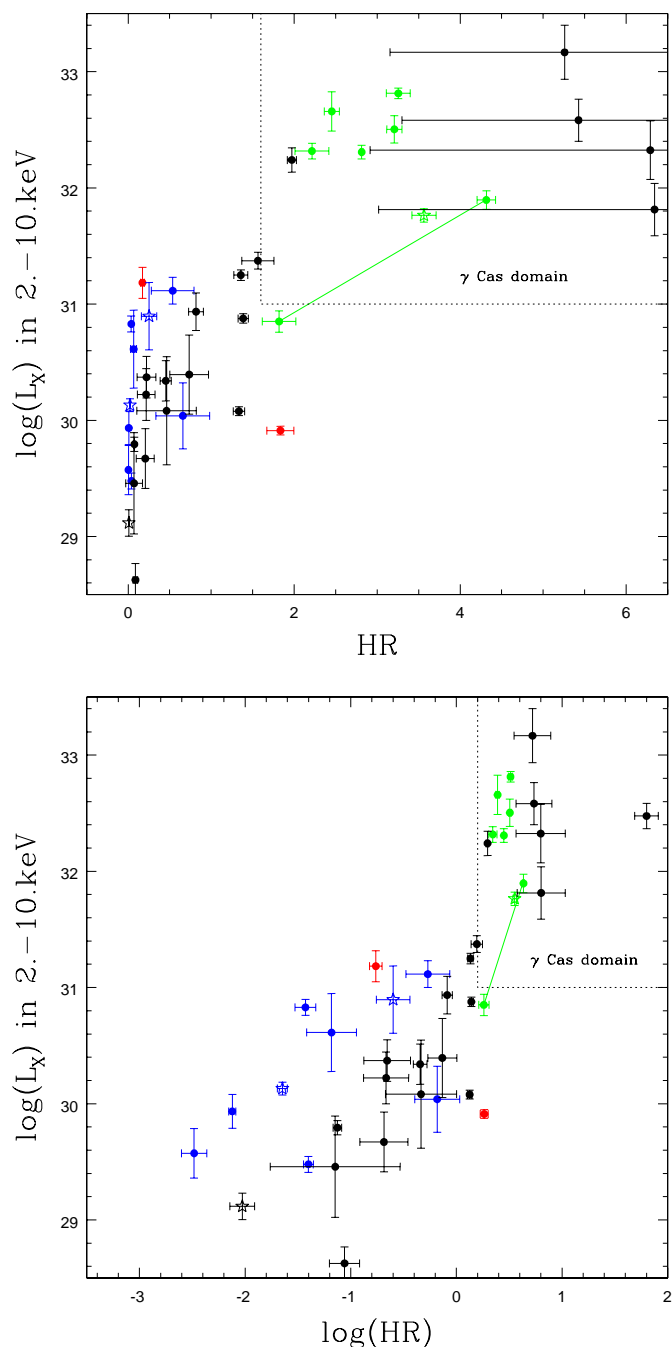
Fig. 3. Comparison of the X-ray luminosities in the hard (2.0–10.0 keV) energy range and the hardness ratios. Symbols are the same as in Fig. 2.

– V782 Cas: this star displays a high peculiar space velocity of 102 km s^{-1} (Berger & Gies 2001), suggesting that binary evolution affected it. It might either be a kicked binary system, or more classically, a disrupted runaway star.

– V767 Cen: this star displays a very low projected rotational velocity $v\sin(i)$, suggesting that it is seen nearly pole-on, as was subsequently shown by Frémat et al. (2002). A spectropolarimetric FORS observation was reported by Schöller et al. (2017), with a formal 2–3σ measurement of a weak dipolar magnetic field but larger, 5σ levels are generally required for FORS (see Bagnulo et al. 2015), hence confirmation is awaited. Based on a preliminary assess-

ment of its X-ray properties, Schöller et al. (2017) proposed V767 Cen as a possible γ Cas analog.

– CQ Cir: this star is often referred to as a Herbig Ae/Be PMS star, but it was found to be in the classical IR Be region by Mathew et al. (2008), who explained this oddity as due to a peculiar evolution scenario in which an HAeBe star looses its disk and therefore dereddens to a classical Be location. However, the observed X-ray luminosity is at least two orders of magnitudes above that emitted by the most extreme Herbig Ae/Be stars (Stelzer et al. 2006).

– V771 Sgr

– HD 316568: this star shows a high temperature - hardness ratio, and hard X-ray luminosity, but a slightly lower broadband X-ray luminosity than the other analogs.

– V2156 Cyg

– V810 Cas

Even if none of those stars has an X-ray luminosity typical of HMXBs (which are brighter than 10^{34} erg s^{-1}), we have also attempted a power-law fit: the power-law photon exponent is typical of what is found in the known γ Cas objects ($\Gamma \sim 1.5 - 1.8$) for all but V782 Cas (which has a small $\Gamma \sim 0.8$) and V810 Cas ($\Gamma \sim 1.2$, a value typical of HMXBs). It is certain that these seven objects display a very hard spectrum and intermediate X-ray luminosities, both reminiscent of what is seen in γ Cas analogs.

For simple detections (see section 4.1.2), two sources appear in the range of γ Cas luminosities: HD 90563 and BQ Cru. Doubts have already been detailed in section 3 about the detection of BQ Cru, but the case of HD 90563 is different. Not only does it have an X-ray luminosity in the range of γ Cas analogs, but most of the counts were collected in the hard band: regardless of the EPIC camera, the count rate in 2.0–10.0 keV is at least twice that in the 0.5–2.0 keV energy band. This star must therefore be added to the list of new γ Cas analogs.

γ Cas analogs share several other characteristics that may be taken into account when assessing the likelihood that a star belong to that class. For instance, the presence of a fluorescence iron line next to the thermal lines from ionized iron at 6.7 keV is also obvious in γ Cas analog spectra, although it requires a well-exposed spectrum to be detected (Giménez-García et al. 2015). For our new detections, the iron line complex clearly appears in the spectrum of V782 Cas and there may be hints of its presence for V767 Cen and V810 Cas (the spectral bin around 6 keV appears slighly above the best-fit spectrum). However, there are not enough counts to test for its presence in the other cases with available spectra.

In addition, the spectral fitting of γ Cas analogs often reveals an absorbing column larger than the interstellar one, and this may vary from one observation to the next (e.g., Smith et al. 2012a). Additional absorption is detected for our new detections, except for HD 316568, but other Oe and Be stars also display local absorption: this criterion is thus a (very) loose one.

All γ Cas analogs also exhibit X-ray variability on various timescales, down to timescales that are limited by the count rate (i.e., about 10 seconds for the X-ray brightest ones; Smith et al. 1998; Lopes de Oliveira et al. 2007; Smith et al. 2012a; Hamaguchi et al. 2016). In addition to fast X-ray shot-noise like variability, large amplitude modulations on timescales of one hour or more are ubiquitous (Smith et al. 2016) and long-term variations linked to the disappearance and building-up of
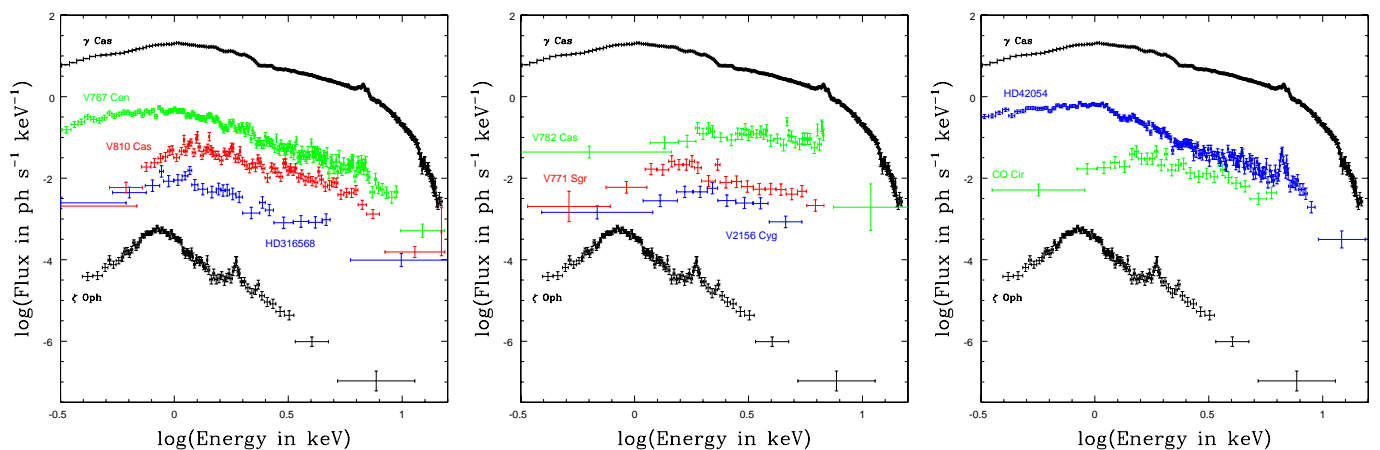
Fig. 4. Spectra of seven new γ Cas analogs and of one candidate, compared to those of γ Cas and ζ Oph. The spectra slopes at high energies clearly are much flatter than for "normal" sources such as ζ Oph. For clarity, the spectra of ζ Oph and V782 Cas have been shifted by –2.5 dex and +1 dex, respectively.
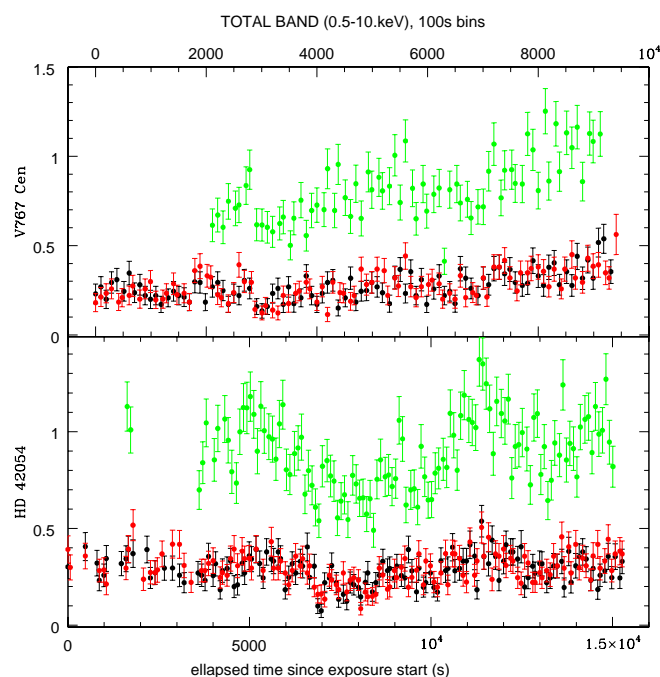

Fig. 5. Background-corrected XMM-*Newton* light curves of V767 Cen and HD 42054, derived from the same extraction regions as the spectra and corrected for the loss of photons due to vignetting, off-axis angle, or other problems such as bad pixels using *epiclccorr*. EPIC-MOS1, MOS2, and pn data are shown in black, red, and green, respectively. Bins with effective exposure times shorter than the total bin length (100 s) are not shown.

the disk have also been detected (Rauw et al. 2018). A correlation between X-ray luminosity and disk density was indeed found by Motch et al. (2015) and Rauw et al. (2018). The presence of short-term variability was assessed when enough counts were present (see the variability flag in Table 1). V767 Cen appears significantly variable, with a strong increasing trend during its exposure (Fig. 5), while V782 Cas, HD 316568, and V810 Cas are not statistically variable. Longer-term variability can be assessed if several exposures separated by weeks, months, or years are available. When this was the case, fluxes (Table 3) or count rates were compared and changes were

detected in all cases: the flux of HD 316568 changes from 4.0 ± 1.3 to $6.5\pm0.6\times10^{-14}$ erg cm^{-2} s^{-1}, the *Swift* count rate[10] of CQ Cir varies between 0.045 ± 0.011 and 0.116 ± 0.008 cts s^{-1}, and the *Swift* count rate[10] of V771 Sgr is found in the interval $0.025\pm0.010 - 0.098\pm0.013$ cts s^{-1}.

Optically, a dense decretion disk seems also required for a star to display a γ Cas behavior. Unfortunately, except for γ Cas and π Aqr, no optical spectra at the exact dates of the X-ray observations are available in the BeSS database for γ Cas analogs. However, available data at other times seem to confirm this tendency (Table 5).

Known γ Cas analogs also display a limited range in spectral type, from late-O to early-B. This is also the case of our new cases, although V782 Cas and V771 Sgr may be of slightly later type than the bulk of γ Cas analogs. We note, however, that the spectral types are quite uncertain for these two stars.

Finally, we examined the rotational velocities. In our sample, the harder emissions are usually reached only for the fastest rotators (left panel of Fig. 6), but there is no formal, significant correlation between rotation velocity and X-ray luminosity overall. For γ Cas objects, the origin of the magnetic field in the star-disk interaction paradigm is essentially unconstrained, but Motch et al. (2015) proposed that the phenomenon appears when the star rotates very close to the critical velocity so that subsurface convecting layers may eventually generate an equatorially condensed magnetic field with no large-scale structure. Measuring the V_{rot}/V_{crit} quantity requires an estimate of the rotation axis inclination, however. Assuming that disk and star rotation axis are coaligned, inclination can be obtained by optical or infrared interferometry measuring the oblateness of the circumstellar disk (see Stee et al. 2012, e.g.). Only few data are available, but in the scantily populated group of Be stars with interferometric measurements, the two most critically rotating Be stars are γ Cas and BZ Cru, and they exhibit the γ Cas phenomenon. Conversely, none of the other Be stars with available X-ray data in this sample exhibits γ Cas-like properties, thus apparently supporting the proposed mechanism.

For our sample, without the knowledge of the inclination, we are left with the comparison of projected rotational velocities. Since the critical velocity depends sensitively on the spectral type (see, e.g., Zorec et al. 2016, and references therein) and γ Cas analogs display spectral types between B2.5 and O9, we compared the $v_{rot} \sin i$ distribution of the γ Cas objects with
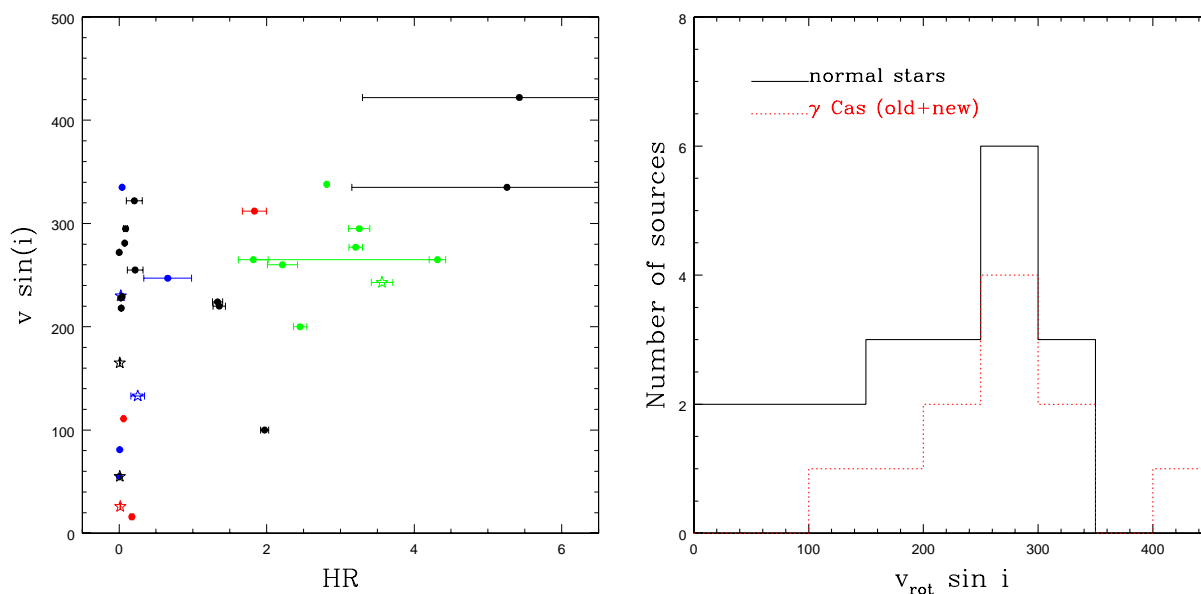
Fig. 6. *Left:* Comparisons of projected rotational velocities (when known, see Table 2) to hardness ratios. Symbols are the same as in Fig. 2. *Right:* Histogram of projected rotational velocities for all γ Cas analogs (previously known ones and new ones) and stars without any γ Cas characteristics but with similar effective temperatures ($\log(T_{eff})$= 4.28 to 4.55).

known rotational velocities to that of the Be stars in our survey in the same range of effective temperatures ($\log(T_{eff})$= 4.28 to 4.55) but do not show any sign of γ Cas activity. Comparing these two samples originating from the same input list and processed in the same manner is probably the best manner to minimize selection effects. The right panel of Fig. 6 shows that γ Cas stars tend to have higher projected rotational velocities than non-γ Cas stars of similar spectral types, thus supporting the idea that high (or critical) rotation may be a key ingredient of the γ Cas phenomenon. However, owing to the small number statistics, the difference is not really statistically significant when formally using a Kolgomorov-Smirnov test.

Although they do not formally fulfill all criteria, some other objects also appear quite remarkable in our sample because of their bright/hard X-ray emission. The first two cases, HD 42054 and V1230 Ori, appear close to the γ Cas domain (Fig. 3), although they display slightly lower hardness ratios ($1 < HR < 1.6$) that reflect plasma temperatures of 2–5 keV. They are also variable, both on short (Table 1) and long (Table 3) timescales. While V1230 Ori is not bright enough to compete with γ Cas objects and some confusion with a nearby active star cannot be totally excluded for it, HD 42054 appears particularly remarkable (with $< L_X(hard) >= 1.8 \times 10^{31}$ erg s^{-1}) and can be considered as a γ Cas candidate. This star, which was the subject of several studies, was not detected to have a sdO companion (Wang et al. 2018) and is not a runaway star (Tetzlaff et al. 2011). Based on its irregular optical variations measured by *Hipparcos*, Rimoldini et al. (2012) found it to be similar to γ Cas, with a probability of 42–86% (depending on the method used). Compared to the bulk of the established γ Cas, it displays somewhat softer X-rays, slightly less intense hard X-ray luminosities, a later spectral type, and smaller $EW(H\alpha)$ (Table 5, Fig. 7), but its spectra clearly show a strong iron line complex (Fig. 4) and remarkable short-term variations (oscillating behavior detected during the XMM-*Newton* exposure, see Fig. 5). It may represent the first case of a low-intensity γ Cas phenomenon.

Two other sources, HD 17505 and EM* MWC 659, have X-ray luminosities in the range $10^{33} - 10^{34}$ erg s^{-1} (Table 4), prob-

ably too high for γ Cas analogs and more similar to HMXB luminosities. HD 17505 is a multiple O-star system, and it remains to be seen how this influences the recorded level of X-ray emission. In any case, the data are scarce for both objects (only a simple detection), therefore more information is required before we definitively conclude on the nature of these two objects.

5. Summary and conclusion

We have performed a survey of Oe and Be stars in the X-ray range using XMM-*Newton*, *Chandra*, and *Swift* data. To this aim, we have cross-correlated the BeSS catalog of Be stars with the 3XMM-DR7, *Chandra*-CXOGSG, and XMM-SL2 catalogs. We also searched for more recent public observations of such stars (not yet included in these catalogs). Some shortcomings are inherent to this approach: the BeSS database may be incomplete, Be phases may be missed for some objects (which would thus not appear in the list of Be stars), some X-ray datasets may not yet be public, and upper limits were not investigated (because of the large variation in quality of such limits between objects and the absence of reliable exposure maps in some cases, such as the XMM slew survey). However, focusing on homogeneous catalogs and secure detections ensures reliable results for the targets under investigation, which is why we preferred this approach.

Overall, 84 matches were found. Nine of these are dubious associations mostly because of the relatively large distance between the Be star and its X-ray counterpart. In 51 cases, enough counts could be extracted to perform a spectral analysis. Using absorbed optically thin thermal models, we derived the X-ray luminosities in several bands, the hardness ratios, the plasma temperature(s), and the local absorption. For the remaining cases, the count rates were converted into broad-band X-ray luminosities. Compared to other surveys of OB stars, our targets show a similar range of X-ray luminosities, but with a substantial contribution of bright and hard (defined as high hardness ratios and/or high temperatures) sources. This is caused by the presence of γ Cas objects. We note, however, that our targets are not split into clear-cut groups in X-ray luminosity versus hardness graphs.

Splitting the targets in categories, we found that O-type stars and magnetic OB stars display the typical characteristics of their classes, while confusion with nearby active stars may become important for the latest stars of our sample, however. On the other hand, the properties of the known γ Cas analogs led us to identify eight new cases. They display high X-ray luminosities ($L_X^{ISM\,cor}(0.5-10.keV) > 4\times10^{31}$ erg s^{-1}, $L_X^{ISM\,cor}(2.-10.keV) > 10^{31}$ erg s^{-1}, $\log(L_X/L_{BOL}) > -6$), high hardness ratios ($HR > 1.6$ or $kT > 5$ keV), and early spectral types. When the information is available, most objects also present the iron line complex in their spectra, evidence of local absorption, short- and/or long-term variations of their X-ray emission, strong emission in Hα, and/or relatively high projected rotational velocities. In addition, one star appears to be in an intermediate stage between "normal" OB stars and γ Cas objects, which could be linked to a low-intensity γ Cas phenomenon, for example, because of a later spectral type and a less dense circumstellar disk. We therefore consider this star as a γ Cas candidate. Finally, two Be stars may be even more luminous, but the lack of detailed information prevents us from drawing secure conclusions regarding their nature.

Further investigation is required to study these new γ Cas analogs and candidate in more detail, as well as the peculiar objects found in our survey. In particular, optical and X-ray monitoring would provide invaluable information to constrain the so-called γ Cas phenomenon.

References

Abt, H. A., Levato, H., & Grosso, M. 2002, ApJ, 573, 359

Antokhin, I. I., Rauw, G., Vreux, J.-M., van der Hucht, K. A., & Brown, J. C. 2008, A&A, 477, 593

Asplund, M., Grevesse, N., Sauval, A.J., & Scott, P. 2009, ARA&A, 47, 481

Bagnulo, S., Landstreet, J. D., Mason, E., et al. 2006, A&A, 450, 777

Bagnulo, S., Fossati, L., Landstreet, J. D., & Izzo, C. 2015, A&A, 583, A115

Baume, G., Vázquez, R. A., Carraro, G., & Feinstein, A. 2003, A&A, 402, 549

Berger, D. H., & Gies, D. R. 2001, ApJ, 555, 364

Berghoefer, T. W., Schmitt, J. H. M. M., Danner, R., & Cassinelli, J. P. 1997, A&A, 322, 167

Bragg, A. E. & Kenyon, S. J. 2002, AJ, 124, 3289.

Capitanio, L., Lallement, R., Vergely, J. L., Elyajouri, M., & Monreal-Ibero, A. 2017, A&A, 606, A65

Chauville, J., Zorec, J., Ballereau, D., et al. 2001, A&A, 378, 861

Claeskens, J.-F., Gosset, E., Nazé, Y., Rauw, G., & Vreux, J.-M. 2011, A&A, 525, A142

Cohen, D. H., Cassinelli, J. P., & MacFarlane, J. J. 1997, ApJ, 487, 867

Currie, T., Hernandez, J., Irwin, J., et al. 2010, ApJS, 186, 191

David, T. J., & Hillenbrand, L. A. 2015, ApJ, 804, 146

de Jager, C., & Nieuwenhuijzen, H. 1987, A&A, 177, 217

Evans, D. S. 1967, Determination of Radial Velocities and their Applications, 30, 57

Frémat, Y., Zorec, J., Hubert, A.-M., et al. 2002, A&A, 385, 986

Gaia Collaboration, Brown, A. G. A., Vallenari, A., et al. 2016, A&A, 595, A2

Gaia Collaboration, Brown, A. G. A., Vallenari, A., et al. 2018, arXiv:1804.09365

Gagné, M., Cohen, D., Owocki, S., Townsley, L., & Broos, P., poster presented at "Contifest, a lifetime of influence", available on http://www2.lowell.edu/workshops/Contifest/talks/Gagne.pdf

Giménez-García, A., Torrejón, J. M., Eikmann, W., et al. 2015, A&A, 576, A108

Gkouvelis, L., Fabregat, J., Zorec, J., et al. 2016, A&A, 591, A140

Głębocki, R., & Gnaciński, P. 2005, 13th Cambridge Workshop on Cool Stars, Stellar Systems and the Sun, 560, 571

Gontcharov, G. A., & Mosenkov, A. V. 2018, MNRAS, 475, 1121

Grunhut, J. H., Wade, G. A., & MiMeS Collaboration 2012, American Institute of Physics Conference Series, 1429, 67

Grunhut, J. H., Wade, G. A., Neiner, C., et al. 2017, MNRAS, 465, 2432

Guarcello, M. G., Prisinzano, L., Micela, G., et al. 2007, A&A, 462, 245

Gudennavar, S. B., Bubbly, S. G., Preethi, K., & Murthy, J. 2012, ApJS, 199, 8

Hamaguchi, K., Oskinova, L., Russell, C. M. P., et al. 2016, ApJ, 832, 140

Huang, W., Gies, D. R., & McSwain, M. V. 2010, ApJ, 722, 605

Hensberge, H., Pavlovski, K., & Verschueren, W. 2000, Star Formation from the Small to the Large Scale, 445, 395

Jaschek, M., & Egret, D. 1982, Be Stars, 98, 261

Kaltcheva, N. T., & Golev, V. K. 2012, PASP, 124, 128

Li, G.-W., Shi, J.-R., Yanny, B., et al. 2018, ApJ, 863, 70

Lopes de Oliveira, R., Motch, C., Smith, M. A., Negueruela, I., & Torrejón, J. M. 2007, A&A, 474, 983

Lopes de Oliveira, R., Smith, M. A., & Motch, C. 2010, A&A, 512, A22

Luri, X., Brown, A. G. A., Sarro, L. M., et al. 2018, arXiv:1804.09376

Maryeva, O. V., Chentsov, E. L., Goranskij, V. P., Dyachenko, V. V., & Karpov, S. V. 2017, Stars: From Collapse to Collapse, 510, 187

Marshall, D. J., Robin, A. C., Reylé, C., Schultheis, M., & Picaud, S. 2006, A&A, 453, 635

Mathew, B., Subramaniam, A., & Bhatt, B. C. 2008, MNRAS, 388, 1879

Mennickent, R. E., Pietrzyński, G., Gieren, W., & Szewczyk, O. 2002, A&A, 393, 887

Meurs, E. J. A., Piters, A. J. M., Pols, O. R., et al. 1992, A&A, 265, L41

Motch, C., Lopes de Oliveira, R., & Smith, M. A. 2015, ApJ, 806, 177

Table 3. Results of the spectral fitting.

# Name	ObsID	N_H^{ISM} $(10^{22}$ cm$^{-2})$	N_H	kT_1 (keV)	$norm_1$ (cm^{-5})	kT_2 (keV)	$norm_2$ (cm^{-5})	kT_3 (keV)	$norm_3$ (cm^{-5})	χ_ν^2(dof)	F_X^{obs}(tot) (erg cm^{-2} s^{-1})	$L_X^{ISM\,cor}$(tot) (erg s^{-1})	$\log(L_X/L_{BOL})$	HR
1 γ Cas	0651670201	0.027	0.104±0.001	15.55±0.15	0.10491±0.00016					3.63(909)	(1.816±0.003)e-10	(7.94±1.67)e32	−5.4136±0.0007	3.246±0.008
1 γ Cas	0651670301	0.027	0.101±0.001	14.34±0.17	0.09293±0.00016					2.82(897)	(1.609±0.003)e-10	(7.03±1.48)e32	−5.4660±0.0008	3.164±0.010
1 γ Cas	0651670401	0.027	0.050±0.001	15.57±0.13	0.12750±0.00018					4.80(921)	(2.258±0.003)e-10	(9.88±2.08)e32	−5.3184±0.0006	2.978±0.008
1 γ Cas	0651670501	0.027	0.099±0.001	14.20±0.14	0.09272±0.00013					3.54(915)	(1.607±0.003)e-10	(7.02±1.48)e32	−5.4668±0.0008	3.145±0.009
1 γ Cas	0743600101	0.027	0.125±0.001	25.26±0.23	0.14451±0.00022					8.64(936)	(2.442±0.003)e-10	(1.07±0.22)e33	−5.2857±0.0005	3.740±0.007
2 Achernar		0.0006	0.024±0.013	0.21±0.02	(2.15±0.29)e-4	0.76±0.04	(1.28±0.15)e-4			1.03(103)	(4.32±0.16)e-13	(9.51±0.57)e28	−8.025±0.016	0.029±0.003
3 V782 Cas		0.30	6.05±1.02	6.85±1.55	(3.23±0.57)e-3					1.52(34)	(2.74±0.44)e-12	(3.03±0.78)e32	−5.25±0.07	63.1±16.2
9 HD 19818		0.010	0.72±0.27	0.54±0.28	(8.55±9.08)e-4					2.38(11)	(3.70±3.70)e-13	(4.31±4.31)e30	−4.42±0.43	0.07±0.10
10 Merope	13	0.013	0.03±0.04	0.765±0.019	(1.18±0.11)e-4					1.62(54)	(2.36±0.09)e-13	(3.27±0.33)e29	−6.869±0.017	0.049±0.004
10 Merope	366	0.013	0.03±0.06	0.63±0.03	(9.97±1.72)e-5					0.79(28)	(1.95±0.17)e-13	(2.72±0.35)e29	−6.95±0.04	0.028±0.004
10 Merope	17250	0.013	0.29±0.06	0.60±0.04	(1.88±0.28)e-4					1.33(29)	(1.99±0.13)e-13	(2.76±0.32)e29	−6.94±0.03	0.043±0.007
10 Merope	17251	0.013	0.06±0.07	0.76±0.04	(1.14±0.16)e-4					1.23(26)	(2.13±0.18)e-13	(2.96±0.37)e29	−6.91±0.04	0.051±0.007
10 Merope	17252	0.013	0.18±0.04	0.61±0.03	(1.49±0.16)e-4					1.26(56)	(2.06±0.10)e-13	(2.85±0.30)e29	−6.93±0.02	0.035±0.004
11 Menkhib	0770990101	0.12	0.055±0.005	0.159±0.002	(2.95±0.14)e-3	0.656±0.004	(1.058±0.014)e-3			7.96(309)	(2.17±0.02)e-12	(6.05±2.38)e31	−6.831±0.004	0.0208±0.0005
11 Menkhib	0770990201	0.12	0.004±0.004	0.193±0.002	(1.81±0.05)e-3	0.739±0.003	(8.92±0.08)e-4			7.53(318)	(2.26±0.02)e-12	(6.21±2.44)e31	−6.820±0.004	0.0243±0.0006
12 λ Eri		0.013	0.07±0.05	0.241±0.019	(4.95±1.89)e-5	1.23±0.13	(2.34±0.44)e-5			1.36(36)	(6.85±0.67)e-14	(5.27±0.69)e29	−7.73±0.04	0.09±0.03
14 V1230 Ori	0212480301	0.023	0.64±0.07	1.05±0.23	(2.13±0.66)e-4	3.33±1.28	(1.18±0.22)e-3			1.13(64)	(1.32±0.09)e-12	(3.03±0.37)e31	−3.76±0.03	1.93±0.20
14 V1230 Ori	0403200101	0.023	0.99±0.09	1.05±0.11	(5.31±1.36)e-4	3.53±0.40	(1.05±0.08)e-3			1.54(95)	(1.25±0.06)e-12	(2.87±0.32)e31	−3.79±0.02	2.07±0.15
14 V1230 Ori	3	0.023	0.45±0.20	1.90±0.27	(4.84±0.64)e-4					1.04(11)	(3.94±0.30)e-13	(9.10±1.15)e30	−4.28±0.03	1.01±0.15
14 V1230 Ori	4	0.023	0.25±0.20	2.28±0.42	(5.05±0.85)e-4					1.17(7)	(4.96±0.47)e-13	(1.15±0.16)e31	−4.18±0.04	1.07±0.23
14 V1230 Ori	18	0.023	0.64±0.04	2.50±0.10	(7.81±0.25)e-4					1.18(139)	(6.48±0.16)e-13	(1.49±0.16)e31	−4.070±0.011	1.86±0.07
14 V1230 Ori	1522	0.023	0.80±0.08	0.96±0.07	(1.44±0.43)e-4	2.65±0.18	(5.75±0.36)e-4			1.14(111)	(5.54±0.20)e-13	(1.27±0.14)e31	−4.138±0.016	1.65±0.09
14 V1230 Ori	2567	0.023	0.36±0.08	2.49±0.18	(5.80±0.42)e-4					1.16(34)	(5.50±0.28)e-13	(1.27±0.14)e31	−4.14±0.02	1.38±0.13
14 V1230 Ori	2568	0.023	0.38±0.09	2.80±0.30	(5.01±0.40)e-4					0.81(29)	(5.00±0.28)e-13	(1.15±0.13)e31	−4.18±0.02	1.64±0.19
14 V1230 Ori	3498	0.023	0.82±0.10	0.93±0.05	(2.15±0.71)e-4	2.46±0.13	(5.63±0.34)e-4			1.08(147)	(5.57±0.13)e-13	(1.28±0.13)e31	−4.135±0.010	1.35±0.06
14 V1230 Ori	3744	0.023	0.96±0.05	0.95±0.03	(2.14±0.40)e-4	2.44±0.08	(7.03±0.24)e-4			1.53(244)	(6.22±0.10)e-13	(1.43±0.15)e31	−4.088±0.007	1.64±0.04
14 V1230 Ori	4373	0.023	0.75±0.04	0.93±0.05	(1.23±0.23)e-4	2.71±0.07	(9.64±0.23)e-4			1.46(286)	(8.86±0.12)e-13	(2.03±0.21)e31	−3.935±0.006	1.87±0.04
14 V1230 Ori	4374	0.023	0.87±0.05	0.91±0.06	(1.77±0.34)e-4	2.24±0.07	(6.34±0.21)e-4			1.58(225)	(5.48±0.08)e-13	(1.26±0.13)e31	−4.142±0.006	1.39±0.04
14 V1230 Ori	4395	0.023	0.93±0.07	0.99±0.04	(2.07±0.52)e-4	2.71±0.10	(7.69±0.30)e-4			1.24(202)	(7.17±0.15)e-13	(1.65±0.17)e31	−4.026±0.009	1.90±0.06
14 V1230 Ori	4396	0.023	0.75±0.05	0.96±0.05	(1.08±0.21)e-4	2.56±0.08	(6.81±0.20)e-4			1.31(243)	(6.19±0.09)e-13	(1.42±0.15)e31	−4.090±0.006	1.68±0.04
14 V1230 Ori	4473	0.023	0.24±0.13	2.48±0.24	(5.12±0.56)e-4					1.11(26)	(5.25±0.31)e-13	(1.21±0.14)e31	−4.16±0.03	1.17±0.14
14 V1230 Ori	4474	0.023	0.26±0.12	2.95±0.35	(5.15±0.53)e-4					1.06(29)	(5.60±0.32)e-13	(1.29±0.15)e31	−4.13±0.02	1.51±0.20
14 V1230 Ori	7407	0.023	0.84±0.54	1.34±0.35	(7.16±2.36)e-4					0.88(4)	(4.28±0.75)e-13	(9.90±2.00)e30	−4.25±0.08	0.71±0.25
14 V1230 Ori	7408	0.023	0.23±0.13	2.22±0.29	(4.08±0.48)e-4					1.66(12)	(4.03±0.37)e-13	(9.35±1.28)e30	−4.27±0.04	1.00±0.19
14 V1230 Ori	7409	0.023	0.21±0.11	2.29±0.29	(3.57±0.41)e-4					2.12(12)	(3.51±0.28)e-13	(8.37±1.07)e30	−4.32±0.03	1.02±0.19
14 V1230 Ori	7410	0.023	0.44±0.31	2.03±0.44	(4.72±1.04)e-4					2.87(6)	(3.93±0.50)e-13	(9.08±1.47)e30	−4.29±0.06	1.12±0.33
14 V1230 Ori	7411	0.023	0.14±0.10	2.03±0.33	(3.75±0.40)e-4					0.73(11)	(3.89±0.32)e-13	(9.05±1.18)e30	−4.29±0.04	0.78±0.15
14 V1230 Ori	7412	0.023	0.31±0.13	2.50±0.34	(4.65±0.55)e-4					0.72(13)	(4.57±0.33)e-13	(1.06±0.13)e31	−4.22±0.03	1.29±0.18
14 V1230 Ori	8568	0.023	0.25±0.13	2.27±0.26	(3.81±0.44)e-4					1.18(17)	(3.74±0.26)e-13	(8.64±1.06)e30	−4.31±0.03	1.06±0.16
14 V1230 Ori	8589	0.023	1.17±0.27	0.95±0.21	(4.34±1.95)e-4	3.81±15.52	(1.97±1.03)e-4			0.84(21)	(3.66±0.77)e-13	(8.42±1.96)e30	−4.32±0.09	1.26±0.56
14 V1230 Ori	8895	0.023	0.35±0.18	2.33±0.34	(6.19±0.90)e-4					1.32(11)	(5.75±0.48)e-13	(1.33±0.17)e31	−4.12±0.04	1.24±0.24
14 V1230 Ori	8896	0.023	0.81±0.36	0.85±0.16	(2.45±2.57)e-4	2.50±1.73	(3.36±1.48)e-4			0.73(9)	(4.01±0.71)e-13	(9.28±1.89)e30	−4.28±0.08	1.03±0.35
14 V1230 Ori	8897	0.023	0.46±0.30	2.31±0.41	(4.32±0.98)e-4					1.01(10)	(3.76±0.31)e-13	(8.64±1.13)e30	−4.31±0.04	1.40±0.26
14 V1230 Ori	13637	0.023	1.34±0.14	0.96±0.08	(4.97±1.46)e-4	2.41±0.94	(2.56±0.96)e-4			1.03(41)	(3.47±0.35)e-13	(8.01±1.14)e30	−4.34±0.04	1.16±0.21
14 V1230 Ori	14334	0.023	0.26±0.11	2.90±0.43	(5.11±0.51)e-4					0.74(19)	(5.52±0.47)e-13	(1.27±0.17)e31	−4.14±0.04	1.48±0.22
14 V1230 Ori	14335	0.023	1.18±0.14	0.86±0.07	(3.64±1.27)e-4	2.23±0.23	(5.27±0.69)e-4			0.79(54)	(4.79±0.30)e-13	(1.10±0.13)e31	−4.20±0.03	1.37±0.15
14 V1230 Ori	15546	0.023	1.06±0.26	1.18±0.20	(3.65±2.47)e-4	3.08±10.54	(2.95±1.74)e-4			1.05(31)	(4.26±0.77)e-13	(9.78±2.03)e30	−4.25±0.08	1.53±0.59
14 V1230 Ori	17735	0.023	0.53±0.05	2.58±0.11	(7.58±0.29)e-4					1.28(147)	(6.71±0.15)e-13	(1.54±0.15)e31	−4.055±0.010	1.76±0.07

Table 3. Continued.

# Name	ObsID	$N_{\rm H}^{ISM}$ (10^{22} cm^{-2})	$N_{\rm H}$ (10^{22} cm^{-2})	kT_1 (keV)	$norm_1$ (cm^{-5})	kT_2 (keV)	$norm_2$ (cm^{-5})	kT_3 (keV)	$norm_3$ (cm^{-5})	χ^2_γ(dof)	$F_{\rm X}^{obs}$(tot) (erg cm^{-2} s^{-1})	$L_{\rm X}^{ISM\,cor}$(tot) (erg s^{-1})	log($L_{\rm X}/L_{\rm BOL}$)	HR
15 43 Ori	0212480301	0.032	0.22±0.04	0.248±0.014	(8.29±2.55)e-4	0.77±0.05	(2.76±0.42)e-4	2.34±0.34	(3.64±0.32)e-4	1.29(101)	(1.07±0.05)e-12	(2.90±0.78)e31	−6.07±0.02	0.24±0.04
15 43 Ori	0403200101	0.032	0.22±0.02	0.245±0.007	(8.18±1.07)e-4	0.77±0.02	(2.62±0.19)e-4	1.88±0.30	(1.31±0.14)e-4	1.80(182)	(7.92±0.12)e-13	(2.16±0.58)e31	−6.199±0.007	0.103±0.014
15 43 Ori	3	0.032	0.000±0.017	0.60±0.04	(2.08±0.16)e-4	1.58±0.12	(1.80±0.20)e-4			1.66(43)	(6.31±0.50)e-13	(1.70±0.47)e31	−6.30±0.03	0.12±0.02
15 43 Ori	4	0.032	0.000±0.019	0.72±0.06	(2.18±0.19)e-4	2.61±0.34	(3.95±0.39)e-4			0.53(35)	(9.47±0.50)e-13	(2.52±0.68)e31	−6.13±0.02	0.35±0.04
15 43 Ori	2567	0.032	0(fixed)	0.71±0.06	(2.43±0.26)e-4	3.73±1.70	(6.75±0.46)e-5			0.59(12)	(5.99±0.98)e-13	(1.62±0.50)e31	−6.32±0.07	0.13±0.12
15 43 Ori	2568	0.032	0.00±0.05	0.62±0.06	(2.61±0.49)e-4	2.99±2.73	(9.91±3.20)e-5			1.34(22)	(6.47±1.17)e-13	(1.75±0.56)e31	−6.29±0.08	0.13±0.05
15 43 Ori	4473	0.032	0.40±0.17	0.25±0.04	(2.01±1.55)e-3	1.57±0.33	(1.38±0.24)e-4			1.23(28)	(5.93±1.35)e-13	(1.63±0.57)e31	−6.32±0.10	0.08±0.04
15 43 Ori	4474	0.032	0.09±0.02	1.01±0.04	(4.18±0.50)e-4	7.73±0.50	(3.19±0.07)e-3			1.17(243)	(5.98±0.11)e-12	(1.54±0.41)e32	−5.346±0.007	1.84±0.05
15 43 Ori	7407	0.032	0(fixed)	0.31±0.04	(2.92±0.51)e-4	1.14±0.10	(1.64±0.22)e-4			0.61(14)	(6.00±0.39)e-13	(1.65±0.45)e31	−6.32±0.03	0.060±0.013
15 43 Ori	7408	0.032	0.67±0.36	0.21±0.04	(8.36±1.38)e-3	1.59±1.75	(1.49±2.07)e-4			0.60(6)	(6.55±0.60)e-13	(1.80±0.50)e31	−6.28±0.04	0.076±0.013
15 43 Ori	7409	0.032	0.00±0.04	0.60±0.05	(2.57±0.40)e-4	2.81±1.87	(1.05±0.32)e-4			0.69(43)	(6.39±1.33)e-13	(1.73±0.58)e31	−6.29±0.09	0.13±0.03
15 43 Ori	7410	0.032	0(fixed)	0.81±0.13	(1.96±0.35)e-4	2.01±7.48	(1.33±0.92)e-4			1.17(6)	(5.57±0.75)e-13	(1.50±0.45)e31	−6.36±0.06	0.16±0.07
15 43 Ori	7411	0.032	0(fixed)	0.63±0.16	(2.20±0.22)e-4	2.38±0.61	(2.50±0.37)e-4			1.54(20)	(7.46±0.45)e-13	(2.00±0.55)e31	−6.23±0.03	0.23±0.05
15 43 Ori	7412	0.032	0.52±0.14	0.26±0.04	(3.33±3.64)e-3	4.59±9.44	(1.28±0.39)e-4			1.34(17)	(7.48±4.00)e-13	(2.03±1.21)e31	−6.23±0.23	0.18±0.15
15 43 Ori	8568	0.032	0.00±0.05	0.64±0.04	(2.51±0.44)e-4	3.75±2.01	(1.42±0.30)e-4			1.45(24)	(7.08±1.50)e-13	(1.91±0.65)e31	−6.25±0.09	0.21±0.07
15 43 Ori	8589	0.032	0.69±0.14	0.23±0.04	(6.42±0.10)e-3	2.10±0.45	(2.36±0.38)e-4			0.70(31)	(7.00±1.84)e-13	(1.90±0.71)e31	−6.26±0.11	0.17±0.06
15 43 Ori	8895	0.032	0.00±0.03	0.75±0.04	(2.33±0.24)e-4	2.63±0.55	(1.34±0.35)e-4			1.96(16)	(6.49±1.40)e-13	(1.74±0.60)e31	−6.29±0.09	0.17±0.07
15 43 Ori	8896	0.032	0(fixed)	0.73±0.09	(2.62±0.25)e-4	2.54±0.84	(1.94±0.44)e-4			0.63(19)	(7.82±0.45)e-13	(2.10±0.57)e31	−6.21±0.02	0.20±0.04
15 43 Ori	8897	0.032	0(fixed)	0.64±0.08	(2.46±0.25)e-4	2.63±0.71	(1.91±0.38)e-4			1.00(17)	(7.38±0.50)e-13	(1.99±0.54)e31	−6.23±0.03	0.20±0.04
16 HD 42054	0402121401	0.006	0.001±0.003	0.93±0.03	(1.33±0.11)e-4	4.53±0.18	(1.58±0.03)e-3			1.21(448)	(2.74±0.04)e-12	(3.75±0.34)e31	−5.319±0.006	1.23±0.03
16 HD 42054	11021	0.006	0.000±0.012	1.02±0.06	(1.23±0.12)e-4	5.51±0.51	(1.15±0.05)e-3			1.04(213)	(2.15±0.06)e-12	(2.94±0.27)e31	−5.425±0.012	1.39±0.07
16 HD 42054	12226	0.006	0.00±0.02	1.59±0.23	(3.56±1.49)e-4	8.58±2.10	(8.00±1.33)e-4			1.10(51)	(1.91±0.18)e-12	(2.61±0.34)e31	−5.48±0.04	1.46±0.20
17 PZ Gem	0670080301	0.085	0.31±0.02	16.18±4.18	(7.12±0.12)e-4					1.00(394)	(1.14±0.02)e-12	(9.66±1.77)e31	−6.138±0.008	4.32±0.11
17 PZ Gem	0760220601	0.085	0(fixed)	5.79±0.89	(7.80±0.29)e-5					1.03(81)	(1.25±0.09)e-13	(1.10±0.22)e31	−7.08±0.03	1.82±0.20
20 15 Mon	0011420101	0.007	0.188±0.011	0.055±0.004	0.37±0.28	0.229±0.003	(2.75±0.20)e-3	0.86±0.06	(8.01±1.43)e-5	1.79(191)	(1.52±0.04)e-12	(1.55±0.44)e31	−6.363±0.011	0.0071±0.0009
20 15 Mon	5401	0.007	0(fixed)	0.201±0.016	(1.21±0.09)e-3	0.66±0.11	(1.62±0.40)e-4			1.22(43)	(1.29±0.07)e-12	(1.32±0.38)e31	−6.43±0.02	0.0079±0.0016
20 15 Mon	6247	0.007	0(fixed)	0.197±0.018	(1.18±0.11)e-3	0.57±0.10	(2.21±1.05)e-4			1.10(36)	(1.35±0.07)e-12	(1.38±0.40)e31	−6.41±0.02	0.0067±0.0014
20 15 Mon	6248	0.007	0(fixed)	0.22±0.03	(1.15±0.24)e-3	0.86±0.14	(1.70±0.79)e-4			1.11(8)	(1.38±0.19)e-12	(1.41±0.45)e31	−6.40±0.06	0.016±0.009
21 19 Mon		0.020	0.000±0.009	0.25±0.02	(3.10±0.37)e-5					1.51(10)	(2.96±0.58)e-14	(5.43±1.39)e29	−7.94±0.09	0.0009±0.0005
22 HD 57682		0.088	0.000±0.002	0.78±0.02	(1.56±0.08)e-4	1.77±0.19	(1.60±0.14)e-4			1.39(134)	(4.60±0.22)e-13	(1.04±0.29)e32	−6.56±0.02	0.17±0.02
23 BN Gem		0.019	0.008±0.033	0.25±0.03	(2.17±0.71)e-5	5.69±3.25	(2.00±0.41)e-5			1.25(13)	(5.25±0.60)e-14	(2.76±1.53)e30	−7.25±0.05	0.66±0.32
24 V392 Pup	0694730301	0.006	0.07±0.06	0.07±0.02	(3.30±6.33)e-4	0.49±0.05	(2.15±0.50)e-5			0.92(46)	(3.46±0.77)e-14	(1.75±0.40)e29	−6.87±0.10	0.014±0.005
24 V392 Pup	0694730401	0.006	0.53±0.19	0.28±0.07	(1.30±1.04)e-4					0.91(16)	(2.84±1.20)e-14	(1.43±0.61)e29	−6.96±0.18	0.007±0.005
25 V374 Car	0113890601	0.054	0.05±0.04	1.03±0.17	(2.09±0.57)e-5	12.81±25.36	(1.05±0.13)e-4			0.88(34)	(2.18±0.69)e-13	(2.86±1.01)e30	−6.70±0.14	1.76±1.13
25 V374 Car	0113891001	0.054	0.009±0.018	3.71±0.47	(1.19±0.05)e-4					0.93(78)	(1.66±0.12)e-13	(2.20±0.39)e30	−6.81±0.03	1.29±0.17
25 V374 Car	0113891101	0.054	0.011±0.033	4.26±1.01	(7.95±0.55)e-5					1.18(34)	(1.17±0.12)e-13	(1.54±0.29)e30	−6.97±0.04	1.47±0.23
25 V374 Car	0126511201	0.054	0.000±0.013	3.83±0.34	(1.31±0.05)e-4					0.93(103)	(1.86±0.12)e-13	(2.45±0.42)e30	−6.76±0.03	1.31±0.06
25 V374 Car	0134531201	0.054	0.000±0.011	4.09±0.50	(8.92±0.34)e-5					0.87(81)	(1.30±0.07)e-13	(1.72±0.29)e30	−6.92±0.02	1.39±0.13
25 V374 Car	0134531301	0.054	0.02±0.04	4.22±1.09	(9.26±0.72)e-5					1.35(32)	(1.35±0.13)e-13	(1.77±0.33)e30	−6.91±0.04	1.49±0.24
25 V374 Car	0134531501	0.054	0.000±0.014	3.61±0.42	(1.01±0.04)e-4					1.02(74)	(1.40±0.10)e-13	(1.86±0.33)e30	−6.88±0.03	1.24±0.15
25 V374 Car	65	0.054	0.00±0.04	5.08±2.88	(1.46±0.13)e-4					1.47(7)	(2.29±0.39)e-13	(3.02±0.71)e30	−6.67±0.07	1.64±0.49
25 V374 Car	66	0.054	0.00±0.04	3.04±0.72	(1.03±0.10)e-4					0.54(7)	(1.34±0.21)e-13	(1.78±0.40)e30	−6.90±0.07	1.04±0.32
25 V374 Car	1229	0.054	0.00±0.08	3.36±0.85	(8.71±1.23)e-5					3.84(6)	(1.18±0.24)e-13	(1.55±0.40)e30	−6.96±0.09	1.16±0.35
25 V374 Car	1232	0.054	0.00±0.06	3.37±1.03	(1.33±0.16)e-4					1.21(6)	(1.79±0.30)e-13	(2.38±0.55)e30	−6.78±0.07	1.16±0.19
25 V374 Car	1458	0.054	0.05±0.07	2.92±0.91	(1.21±0.13)e-4					0.88(10)	(1.49±0.20)e-13	(1.98±0.41)e30	−6.86±0.06	1.08±0.31
28 HD 93190	9484	0.92	0.18±0.21	0.76±0.18	(3.42±1.28)e-5					1.90(5)	(1.27±0.35)e-14	(6.64±4.54)e31	−8.18±0.12	0.07±0.04
29 HD 93843	9508	0.15	0.50±0.15	0.24±0.03	(9.04±7.19)e-4	1.05±0.16	(4.05±1.54)e-5			0.92(26)	(1.27±0.60)e-13	(1.81±1.32)e32	−6.84±0.21	0.043±0.017
29 HD 93843	9857	0.15	0.32±0.18	0.15±0.05	(0.73±1.60)e-3	0.61±0.08	(1.30±0.47)e-4			1.32(15)	(1.34±0.39)e-13	(1.98±1.24)e32	−6.82±0.13	0.031±0.011
30 HD 305891	0152570101	0.92	0.55±0.15	0.71±0.13	(1.35±0.60)e-4					1.35(16)	(3.22±0.56)e-14	(9.05±5.31)e31	−5.37±0.08	0.11±0.03
32 V863 Cen		0.006	0.03±0.02	0.23±0.03	(3.52±0.82)e-5	1.00±0.07	(2.42±0.30)e-5			0.88(34)	(7.27±0.53)e-14	(9.21±0.86)e28	−7.20±0.03	0.060±0.012
33 δ Cen		0.007	0.001±0.014	0.19±0.09	(0.35±1.42)e-4	0.70±0.07	(2.25±1.07)e-5			0.89(26)	(7.43±0.95)e-14	(1.49±0.27)e29	−8.35±0.06	0.022±0.006
34 BZ Cru		0.20	0.079±0.003	0.97±0.03	(1.40±0.09)e-4	13.33±0.22	(7.21±0.02)e-3			1.54(815)	(1.199±0.004)e-11	(2.76±0.37)e32	−5.6930±0.0014	2.814±0.014
37 HD 119682	0087940201	0.20	0.014±0.008	8.12±0.34	(1.169±0.013)e-3					1.21(471)	(1.89±0.03)e-12	(7.68±2.85)e32	−5.558±0.007	2.26±0.04
37 HD 119682	0551000201	0.20	0.025±0.008	8.41±0.53	(7.05±0.09)e-4					1.10(443)	(1.14±0.02)e-12	(4.63±1.72)e32	−5.778±0.008	2.34±0.05
37 HD 119682	8929	0.20	0.00±0.03	9.92±3.03	(1.13±0.04)e-3					0.89(56)	(1.90±0.13)e-12	(7.68±2.90)e32	−5.56±0.03	2.39±0.15
37 HD 119682	10834	0.20	0.00±0.03	12.01±2.92	(8.64±0.28)e-4					1.20(89)	(1.46±0.08)e-12	(5.88±2.20)e32	−5.67±0.02	2.56±0.19
37 HD 119682	10835	0.20	0.00±0.04	9.47±2.49	(8.44±0.33)e-4					1.14(44)	(1.41±0.60)e-12	(5.69±3.21)e32	−5.69±0.18	2.35±1.05
37 HD 119682	10836	0.20	0(fixed)	17.01±7.56	(1.02±0.05)e-3					0.78(52)	(1.72±0.08)e-12	(6.91±2.58)e32	−5.60±0.02	2.81±0.23

Table 3. Continued.

# Name	ObsID	N_H^{ISM}	N_H	kT_1	$norm_1$	kT_2	$norm_2$	kT_3	$norm_3$	χ_ν^2(dof)	F_X^{obs}(tot)	$L_X^{ISM\,cor}$(tot)	$\log(L_X/L_{BOL})$	HR
		$(10^{22}$ cm$^{-2})$		(keV)	(cm^{-5})	(keV)	(cm^{-5})	(keV)	(cm^{-5})		(erg cm^{-2} s^{-1})	(erg s^{-1})		
38 μ Cen		0.008	0.063±0.013	0.257±0.009	(1.50±0.16)e-4	1.27±0.04	(8.29±0.56)e-5			1.53(95)	(2.35±0.09)e-13	(6.87±0.44)e29	−7.496±0.017	0.099±0.011
39 V767 Cen		0.043	0.067±0.011	0.25±0.02	(1.40±0.36)e-4	6.44±0.26	(1.85±0.03)e-3			1.11(432)	(3.09±0.05)e-12	(2.62±0.63)e32	−5.365±0.007	1.97±0.05
40 CQ Cir		0.28	0.70±0.32	8.66±7.95	(3.11±0.53)e-3					1.03(50)	(4.27±1.63)e-12	(1.75±0.93)e33	−4.30±0.17	5.26±2.10
41 V1040 Sco		0.067	0.07±0.06	0.46±0.37	(1.99±1.85)e-5	6.40±1.12	(3.02±0.13)e-4			1.13(78)	(5.07±0.29)e-13	(1.26±0.10)e30	−6.48±0.02	1.83±0.16
42 δ Sco		0.087	0.000±0.004	0.227±0.003	(7.09±0.21)e-4	0.683±0.013	(1.13±0.07)e-4			1.56(167)	(6.62±0.13)e-13	(2.59±0.71)e30	−7.860±0.009	0.0090±0.0007
43 ζ Oph	2571	0.12	0.02±0.06	0.16±0.03	(2.54±1.57)e-3	0.62±0.03	(1.52±0.27)e-3	^{a}	^{b}	1.05(81)	(3.79±0.47)e-12	(8.16±1.10)e30	−7.18±0.05	0.043±0.005
43 ζ Oph	4367	0.12	0.18±0.05	0.151±0.011	(8.44±3.79)e-3	0.59±0.02	(2.04±0.29)e-3	^{c}	^{d}	1.27(87)	(3.46±0.17)e-12	(7.55±0.55)e30	−7.22±0.02	0.037±0.003
45 V1075 Sco		0.16	0(fixed)	0.197±0.003	(8.11±0.16)e-4	0.605±0.018	(1.37±0.08)e-4			1.47(165)	(4.96±0.08)e-13	(1.15±0.37)e32	−6.874±0.007	0.0076±0.0006
46 γ Ara		0.061	0.001±0.011	0.185±0.008	(2.03±0.22)e-4	0.741±0.016	(1.74±0.08)e-4	^{e}	^{f}	1.46(211)	(5.40±0.17)e-13	(8.95±1.03)e30	−7.261±0.014	0.075±0.007
47 V750 Ara		0.087	0.193±0.011	9.73±0.73	(1.65±0.02)e-3					1.05(408)	(2.68±0.05)e-12	(4.19±1.14)e32	−5.291±0.008	3.21±0.09
50 Cl* NGC 6383 FJL 24		0.28	0.04±0.41	0.26±0.08	(0.21±2.44)e-4	1.67±0.41	(2.28±0.58)e-5			0.37(17)	(2.77±1.00)e-14	(1.30±0.65)e31	−4.93±0.16	0.22±0.11
51 V3892 Sgr	0201200101	0.48	0(fixed)	6.92±0.40	(1.205±0.014)e-3					1.1(400)	(1.73±0.04)e-12	(3.86±1.10)e32	−5.677±0.010	2.03±0.07
51 V3892 Sgr	0691760101	0.48	0(fixed)	7.17±0.41	(7.81±0.10)e-4					0.99(378)	(1.13±0.02)e-12	(2.51±0.71)e32	−5.863±0.008	2.07±0.05
51 V3892 Sgr	8647	0.48	0.00±0.14	12.18±12.14	(8.08±0.83)e-4					1.37(8)	(1.26±0.13)e-12	(2.71±0.82)e32	−5.83±0.04	2.55±1.11
53 V771 Sgr		0.19	0.97±0.29	8.17±23.2	(2.48±0.37)e-3					1.22(37)	(3.26±1.37)e-12	(2.45±1.19)e32	−4.64±0.18	6.29±3.37
54 HD 316568	0206590201	0.33	0.00±0.06	4.87±1.94	(3.66±0.33)e-5					1.31(11)	(4.89±1.18)e-14	(3.83±2.17)e31	−6.27±0.10	1.61±0.58
54 HD 316568	0402280101	0.33	0(fixed)	3.72±0.58	(5.47±0.28)e-5					0.87(41)	(6.48±0.58)e-14	(5.21±2.71)e31	−6.14±0.04	1.27±0.20
54 HD 316568	4547	0.33	0(fixed)	5.73±7.41	(2.57±0.37)e-5					1.15(3)	(3.64±1.27)e-14	(2.81±1.74)e31	−6.40±0.15	1.81±1.28
55 ALS 4570		1.00	0.01±0.16	0.31±0.04	(6.01±4.80)e-4	2.61±0.21	(2.69±0.16)e-4			1.10(83)	(2.57±0.36)e-13	(1.12±0.38)e33	−8.01±0.06	0.18±0.06
56 Cl* NGC 6530 ZCW 175	0008820101	0.24	0(fixed)	2.27±0.41	(2.93±0.29)e-5					1.36(15)	(2.93±0.40)e-14	(5.09±1.42)e30	−5.89±0.06	0.72±0.21
56 Cl* NGC 6530 ZCW 175	3754	0.24	0.53±0.19	0.96±0.11	(1.43±0.40)e-5					1.16(11)	(9.07±1.22)e-15	(1.68±0.47)e30	−6.37±0.06	0.21±0.05
57 HD 164906	0008820101	0.26	0.58±0.14	0.78±0.08	(6.06±1.82)e-5					1.97(18)	(3.16±0.40)e-14	(8.66±2.68)e30	−7.48±0.05	0.14±0.04
57 HD 164906	0720540401	0.26	0.79±0.12	0.73±0.13	(9.09±3.20)e-5					1.60(20)	(3.45±0.62)e-14	(9.16±3.05)e30	−7.45±0.08	0.16±0.05
57 HD 164906	0720540501	0.26	0.70±0.11	0.78±0.07	(8.23±1.67)e-5					1.64(26)	(3.77±0.38)e-14	(9.84±2.94)e30	−7.42±0.04	0.16±0.04
57 HD 164906	0720540601	0.26	0.000±0.009	2.00±0.18	(5.26±0.39)e-5					1.72(32)	(5.01±0.68)e-14	(1.24±0.39)e31	−7.32±0.06	0.58±0.13
57 HD 164906	977	0.26	0.00±0.21	0.72±0.15	(5.13±3.13)e-6					0.49(1)	(6.41±4.00)e-15	(2.15±1.47)e30	−8.08±0.27	0.04±0.02
58 Cl* NGC 6530 ZCW 221	0008820101	0.21	0.06±0.09	2.57±0.75	(4.61±0.58)e-5					1.13(14)	(4.76±0.68)e-14	(1.19±0.38)e31	−5.58±0.06	0.93±0.22
58 Cl* NGC 6530 ZCW 221	0720540401	0.21	0.05±0.12	2.20±0.52	(5.61±0.75)e-5					0.77(14)	(5.47±0.61)e-14	(1.40±0.43)e31	−5.51±0.05	0.74±0.25
58 Cl* NGC 6530 ZCW 221	0720540501	0.21	0.00±0.02	2.84±0.31	(1.22±0.06)e-4					1.15(57)	(1.37±0.11)e-13	(3.47±1.03)e31	−5.11±0.03	0.96±0.14
58 Cl* NGC 6530 ZCW 221	0720540601	0.21	0(fixed)	2.09±0.25	(5.64±0.43)e-5					1.48(27)	(5.64±0.47)e-14	(1.48±0.44)e31	−5.48±0.04	0.63±0.10
59 Cl* NGC 6530 ZCW 228	0008820101	0.23	0.00±0.02	2.07±0.33	(7.28±0.55)e-5					0.90(25)	(7.15±0.67)e-14	(1.25±0.33)e31	−5.51±0.04	0.62±0.11
59 Cl* NGC 6530 ZCW 228	0720540401	0.23	0.00±0.18	1.27±0.16	(2.67±0.58)e-5					1.20(13)	(2.91±0.59)e-14	(5.63±1.78)e30	−5.85±0.09	0.21±0.07
59 Cl* NGC 6530 ZCW 228	0720540601	0.23	0(fixed)	1.95±0.14	(7.32±0.45)e-5					1.24(41)	(7.12±0.50)e-14	(1.26±0.32)e31	−5.50±0.03	0.56±0.08
59 Cl* NGC 6530 ZCW 228	977	0.23	0.00±0.04	1.60±0.08	(2.88±0.23)e-5					1.73(15)	(2.82±0.46)e-14	(5.15±1.51)e30	−5.89±0.07	0.39±0.09
59 Cl* NGC 6530 ZCW 228	3754	0.23	0.00±0.08	1.64±0.43	(1.06±0.24)e-5					0.72(31)	(1.03±0.20)e-14	(1.87±0.58)e30	−6.33±0.08	0.41±0.13
59 Cl* NGC 6530 ZCW 228	4444	0.23	0.00±0.35	1.87±0.54	(1.41±0.33)e-5					0.93(9)	(1.36±0.33)e-14	(2.42±0.83)e30	−6.22±0.11	0.53±0.34
60 V4379 Sgr		0.043	0(fixed)	2.30±0.49	(2.59±0.27)e-3					1.16(66)	(3.12±0.40)e-12	(5.82±4.36)e30	−4.28±0.06	0.74±0.23
63 BD-13 4928	0605130101	0.20	0.82±0.16	0.24±0.05	(3.81±3.83)e-4	2.13±0.45	(4.87±0.67)e-5			0.68(42)	(5.01±1.30)e-14	(3.73±1.20)e31	−6.22±0.11	0.54±0.26
69 HD 190864		0.37	0.37±0.06	0.25±0.02	(7.08±2.61)e-4					1.32(64)	(7.32±1.03)e-14	(1.14±0.51)e32	−7.04±0.06	0.0033±0.0009
74 HD 198931		0.25	1.12±0.15	0.69±0.11	(1.02±0.33)e-4					1.19(14)	(2.57±0.75)e-14	(2.74±1.40)e30	−6.88±0.13	0.21±0.11
75 V2156 Cyg		0.19	2.44±0.91	2.63±2.14	(1.25±0.61)e-3					1.11(6)	(6.88±2.72)e-13	(7.53±3.34)e31	−5.30±0.17	6.34±3.33
76 Alfirk	0300490201	0.004	0.005±0.002	0.207±0.003	(5.76±0.15)e-4	0.700±0.008	(2.24±0.05)e-4			2.14(208)	(9.49±0.12)e-13	(1.27±0.27)e30	−6.920±0.005	0.0178±0.0008
76 Alfirk	0300490301	0.004	0.000±0.002	0.197±0.003	(4.90±0.10)e-4	0.648±0.010	(2.07±0.06)e-4			1.96(200)	(8.20±0.12)e-13	(1.10±0.23)e30	−6.983±0.006	0.0152±0.0007
76 Alfirk	0300490401	0.004	0.011±0.003	0.197±0.003	(5.49±0.16)e-4	0.643±0.010	(2.25±0.07)e-4			1.79(200)	(8.67±0.12)e-13	(1.16±0.24)e30	−6.958±0.006	0.0153±0.0007
76 Alfirk	0300490501	0.004	0.008±0.002	0.201±0.003	(5.39±0.14)e-4	0.651±0.011	(2.09±0.06)e-4			1.71(198)	(8.52±0.11)e-13	(1.16±0.24)e30	−6.966±0.006	0.0150±0.0006
79 π Aqr		0.036	0.226±0.003	11.51±0.25	(6.37±0.03)e-3					1.41(819)	(1.055±0.004)e-11	(7.44±0.99)e31	−5.5918±0.0016	3.56±0.14
82 BD+61 2355		0.16	0.64±2.63	0.41±2.42	(0.82±9.50)e-4					4.30(3)	(2.01±2.01)e-14	(1.10±1.11)e30	−5.84±0.43	0.03±0.04
83 V810 Cas		0.18	0.31±0.04	62.97±31.30	(1.00±0.04)e-3					1.30(71)	(1.38±0.35)e-12	(4.55±1.91)e32	−5.17±0.11	5.43±2.13

Notes. ^{a} 1.18±0.07, ^{b} (6.02±0.89)e-4, ^{c} 1.13±0.24, ^{d} (3.94±0.98)e-4, ^{e} 1.58±0.10, and ^{f} (8.27±0.74)e-5
Whenever several observations were fitted, the second column provides the corresponding ObsID. The spectral models are of the form $tbabs \times phabs \times \sum apec$. The interstellar columns are derived from the color excesses of Table 2 using the formula of Gudennavar et al. (2012). The hardness ratios are defined by $HR = F_X^{ISM\,cor}(hard)/F_X^{ISM\,cor}(soft)$, with soft and hard energy bands being defined as 0.5–2.0 keV and 2.0–10.0 keV, respectively (the total band being 0.5–10.0 keV). Errors correspond to 1σ uncertainties. For the X-ray luminosities, they combine the distance errors (see Table 2) with errors on X-ray fluxes (derived from the "flux err" command in Xspec), but do not integrate the impact of model choices; errors on $\log(L_X/L_{BOL})$, however, do not depend on distance and reflect only X-ray flux uncertainties.

Table 4. X-ray luminosities in 0.5–10.0 keV, corrected for interstellar absorption, for the simple detection cases (see Section 4.1.2 for details).

#	Name	N_H^{ISM} $(10^{22}\,\mathrm{cm}^{-2})$	$L_X^{ISM\,cor}$ (min..max ± error) $(\mathrm{erg\,s}^{-1})$	$\log(L_X/L_{BOL})$ (min..max ± error)
4	Cl* NGC 869 LAV 1039	0.37	(0.4..1.3±0.7)e30	-7.1..-6.7±0.2
5	NGC 869 1164	0.39	(0.2..1.2±1.1)e31	-4.9..-4.1±0.4
6	HD 14162	0.39	(0.6..2.0±1.5)e30	-8.7..-8.2±0.2
7	Cl* NGC 884 LAV 1703	0.41	(1.1..2.7±1.2)e31	-6.0..-5.6±0.2
8	HD 17505	0.47	(0.7..1.0±0.8)e34	-6.1..-5.9±0.2
13	25 Ori	0.016	(0.5..1.9±0.9)e29	-8.7..-8.1±0.2
18	Cl* NGC 2244 PS 26	0.16	(4.1..6.1±1.9)e29	-5.7..-5.6±0.1
19	Cl* NGC 2244 JOHN 33	0.23	(2.2..4.2±0.9)e30	-5.52..-5.25±0.06
26	HD 90563	0.42	(2.0..4.4±3.3)e32	-6.0..-5.7±0.1
31	Phecda	0.0006	(0.4..4.5±2.3)e29	-6.9..-5.8±0.2
35	BQ Cru	0.58	(2.7..6.1±1.7)e32	-4.2..-3.9±0.1
36	HD 117357	0.22	(3.1..5.9±5.8)e30	-7.2..-6.9±0.3
44	HD 153295	0.34	<5.4e32	<-5.0
48	α Ara	0.004	(1.2..6.5±2.9)e30	-6.9..-6.1±0.2
49	V864 Ara	0.035	(0.6..2.4±1.1)e31	-5.1..-4.5±0.2
58	Cl* NGC 6530 ZCW 221	0.21	(1.0..1.8±0.7)e30	-6.6..-6.4±0.1
61	HD 165783	0.39	(0.4..1.5±1.3)e31	-7.3..-6.6±0.3
62	Cl* NGC 6611 PPM 38	0.55	(0.2..1.1±0.2)e31	-5.50..-4.80±0.08
64	Cl* NGC 6611 BKP 29783	0.59	(1.4..4.4±0.7)e31	-5.73..-5.24±0.07
65	BD-13 4933	0.67	(1.1..8.0±6.2)e30	-8.3..-7.5±0.2
66	EM* AS 315	0.80	(1.8..8.0±7.7)e31	-7.7..-7.1±0.2
67	CX Dra	0.015	(0.9..5.0±2.1)e31	-6.1..-5.3±0.2
68	HD 344783	0.37	(1.3..3.8±4.2)e31	-6.8..-6.3±0.2
70	HD 228438	0.40	(1.0..2.4±1.6)e31	-7.8..-7.5±0.2
71	HD 228860	0.65	(0.8..3.0±1.8)e31	-7.7..-7.2±0.2
73	W Del	0.031	(1.0..2.9±0.9)e30	-5.6..-5.1±0.1
77	ϵ Cap	0.004	(1.4..7.8±4.3)e30	-6.6..-5.9±0.2
78	EM Cep	0.13	(2.3..3.0±1.7)e29	-8.1..-8.0±0.1
80	HD 215227	0.15	(0.06..1.1±0.8)e32	-6.9..-5.6±0.2
81	EM* MWC 659	0.26	(0.2..1.1±1.0)e34	-5.0..-4.2±0.2
84	β Scl	0.0006	(1.4..7.7±3.5)e29	-6.3..-5.6±0.2

Notes. The interstellar columns are derived from the color excesses of Table 2 using the formula of Gudennavar et al. (2012). Errors correspond to 1σ uncertainties, combining the distance errors (see Table 2) with errors on maximum count rates or photon fluxes. When there were two detections (XMM-*Newton* and *Chandra* for 25 Ori and XMM-*Newton* slew survey and *Swift* for EM* MWC 659 - for HD 215227, only the XMM-*Newton* detection was considered, not the new *Chandra* one), the range reflects the minimum and maximum fluxes considering available data. For Cl* NGC 6530 ZCW 221, the XMM-*Newton* data (Table 3) most probably refer to a brighter companion (see discussion in Sect. 3), therefore the *Chandra* data reported here reflect the stellar X-ray properties better.

Nazé, Y. 2009, A&A, 506, 1055

Nazé, Y., Broos, P. S., Oskinova, L., et al. 2011, ApJS, 194, 7

Nazé, Y., Petit, V., Rinbrand, M., et al. 2014a, ApJS, 215, 10 (+ erratum ApJS, 224, 13)

Nazé, Y., Wang, Q. D., Chu, Y.-H., Gruendl, R., & Oskinova, L. 2014b, ApJS, 213, 23

Nazé, Y., Rauw, G., & Cazorla, C. 2017, A&A, 602, L5

Nebot Gómez-Morán, A., Motch, C., Barcons, X., et al. 2013, A&A, 553, A12

Nebot Gómez-Morán, A., Motch, C., Pineau, F.-X., et al. 2015, MNRAS, 452, 884

Neiner, C., de Batz, B., Cochard, F., et al. 2011, AJ, 142, 149

Nieva, M.-F. 2013, A&A, 550, A26

Ochsenbein, F. & Halbwachs, J. L. 1987, Bulletin d'Information du Centre de Donnees Stellaires, 32, 83.

Oskinova, L. M., Sun, W., Evans, C. J., et al. 2013, ApJ, 765, 73

Pallavicini, R., Golub, L., Rosner, R., et al. 1981, ApJ, 248, 279

Piatti, A. E., & Clariá, J. J. 2001, A&A, 370, 931

Rauw, G., Nazé, Y., Spano, M., Morel, T., & ud-Doula, A. 2013, A&A, 555, L9

Rauw, G., Nazé, Y., Wright, N. J., et al. 2015, ApJS, 221, 1

Rauw, G., & Nazé, Y. 2016, Advances in Space Research, 58, 761

Rauw, G., Nazé, Y., Smith, M. A., et al. 2018, arXiv:1802.05512

Rimoldini, L., Dubath, P., Süveges, M., et al. 2012, MNRAS, 427, 2917

Robinson, R. D., Smith, M. A., & Henry, G. W. 2002, ApJ, 575, 435

Rosen, S. R., Webb, N. A., Watson, M. G., et al. 2016, A&A, 590, A1

Royer, F., Zorec, J., & Gómez, A. E. 2007, A&A, 463, 671

Savage, B. D., Massa, D., Meade, M., & Wesselius, P. R. 1985, ApJS, 59, 397

Saxton, R. D., Read, A. M., Esquej, P., et al. 2008, A&A, 480, 611

Schulz, N. S., Testa, P., Huenemoerder, D. P., Ishibashi, K., & Canizares, C. R. 2006, ApJ, 653, 636

Selim, I. M., Essam, A., Hendy, Y. H. M., & Bendary, R. 2016, NRIAG Journal of Astronomy and Geophysics, 5, 16

Silaj, J., & Landstreet, J. D. 2014, A&A, 566, A132

Simón-Díaz, S., & Herrero, A. 2014, A&A, 562, A135

Simón-Díaz, S., Godart, M., Castro, N., et al. 2017, A&A, 597, A22

Schöller, M., Hubrig, S., Fossati, L., et al. 2017, A&A, 599, A66

Smith, M. A., Robinson, R. D., & Corbet, R. H. D. 1998, ApJ, 503, 877

Smith, M. A., & Robinson, R. D. 1999, ApJ, 517, 866

Smith, M. A., Lopes de Oliveira, R., & Motch, C. 2012a, ApJ, 755, 64

Smith, M. A., Lopes de Oliveira, R., Motch, C., et al. 2012b, A&A, 540, A53

Table 5. List of properties of known, new, and candidate γ Cas analogs, along with two other peculiar bright sources.

#	Name	Spectral type	$\log(L_X/L_{BOL})$	$L_X^{ISM\,cor}(tot)$ (erg s^{-1})	$L_X^{ISM\,cor}(hard)$	HR	kT (keV)	var.? short/long	−EW(Hα) (Å)	$v_{rot}\sin i$ (km s^{-1})
Known γ Cas analogs										
1	γ Cas	B0IV-Vpe	−5.39±0.04	(8.50±0.84)e32	(6.51±0.68)e32	3.25±0.14	14–25	y/y	34	295
17	PZ Gem (high)	O9pe	−6.138±0.008	(9.66±1.77)e31	(7.87±1.44)e31	4.32±0.11	16	/y	15	265
34	BZ Cru	B0.5IVpe	−5.6930±0.0014	(2.76±0.37)e32	(2.03±0.27)e32	2.814±0.014	13	y/	32	338
37	HD 119682	B0Ve	−5.63±0.04	(6.67±0.58)e32	(4.79±0.43)e32	2.55±0.13	8–17	y/y	5	200
47	V750 Ara	B2Vne	−5.291±0.008	(4.19±1.14)e32	(3.19±0.87)e32	3.21±0.09	10	y/	31	277
51	V3892 Sgr	Oe	−5.78±0.07	(3.08±0.49)e32	(2.12±0.32)e32	2.24±0.24	7–14	y/y		260
79	π Aqr	B1Ve	−5.5918±0.0016	(7.44±0.99)e31	(5.80±0.77)e31	3.56±0.14	12	y/	3	243
New γ Cas analogs										
3	V782 Cas	B2.5III:[n]e+	−5.25±0.07	(3.03±0.78)e32	(2.99±0.75)e32	63.1±16.2	7	n/	22	
26	HD 90563	B2Ve	−6.0..−5.7	(2.0..4.4)e32					65	
39	V767 Cen	B2Ve	−5.365±0.007	(2.62±0.63)e32	(1.74±0.42)e32	1.97±0.05	6	y/	6	100
40	CQ Cir	B1Ve	−4.30±0.17	(1.75±0.93)e33	(1.47±0.79)e33	5.26±2.10	9	/y		335
53	V771 Sgr	B3/5ne	−4.64±0.18	(2.45±1.19)e32	(2.11±1.23)e32	6.29±3.37	8	/y	53	
54	HD 316568	B2IVpe	−6.26±0.08	(4.04±0.77)e31	(2.43±0.32)e31	1.60±0.23	4–6	n/y		
75	V2156 Cyg	B1.5Vnnpe	−5.30±0.17	(7.53±3.34)e31	(6.51±3.38)e31	6.34±3.33	3		34	
83	V810 Cas	B1npe	−5.139±0.015	(4.84±1.62)e32	(4.11±1.38)e32	5.58±0.30	64	n/	33	422
Candidate γ Cas analog										
16	HD 42054	B4IVe	−5.39±0.05	(3.24±0.34)e31	(1.88±0.13)e31	1.40±0.11	5–9	y/y	12	220
Others										
8	HD 17505	O6.5III((f))n+O8V	−6.1..−5.9	(0.7..1.0)e34						126
81	EM* MWC 659	B0IIIpe	−5.0..−4.2	(0.2..1.1)e34						

Notes. Spectral type and projected rotational velocities are reproduced from Table 2. X-ray properties come from the fits of Table 3 or from Table 4, except when several observations are available, in which case the average values and the dispersions around them are provided. When several thermal components were fit, only the temperature of the hottest one is reported here. For PZ Gem, only the "high" state (i.e., the observation with the highest X-ray luminosity) is reported here. The short-term variability flag comes from Table 1, and the long-term variability flag was set when significant variations of the observed fluxes (see Table 3) or *Swift* count rates are detected. Equivalent widths of the Hα line are estimated from the spectra in the BeSS database taken at the closest time with respect to the X-ray observation(s) (see also Smith et al. 2016 for typical values for the previously known γ Cas analogs). These BeSS observations are rarely simultaneous. In this context, we note that Rauw et al. (2013) reported EW(Hα)=−22Å at the time of the XMM-*Newton* observation in "high" state, while the emission reported here is lower because of its later date.

Smith, M. A., Lopes de Oliveira, R., & Motch, C. 2016, Advances in Space Research, 58, 782

Stee, P., Delaa, O., Monnier, J. D., et al. 2012, A&A, 545, A59

Stelzer, B., Micela, G., Hamaguchi, K., & Schmitt, J. H. M. M. 2006, A&A, 457, 223

Sung, H., Bessell, M. S., & Lee, S.-W. 1997, AJ, 114, 2644

Tetzlaff, N., Neuhäuser, R., & Hohle, M. M. 2011, MNRAS, 410, 190

ud-Doula, A., & Nazé, Y. 2016, Advances in Space Research, 58, 680

ud-Doula, A., Owocki, S. P., & Kee, N. D. 2018, MNRAS, 478, 3049

Uesugi, A., & Fukuda, I. 1970, Contributions from the Institute of Astrophysics and Kwasan Observatory, University of Kyoto, Kyoto: University, Kwasan Observatory, Institute of Astrophysics, 1970,

van Leeuwen, F. 2007, A&A, 474, 653

Wang, S., Liu, J., Qiu, Y., et al. 2016, ApJS, 224, 40

Wang, L., Gies, D. R., & Peters, G. J. 2018, ApJ, 853, 156

Wegner, W. 1993, Acta Astron., 43, 209

Wegner, W. 2007, MNRAS, 374, 1549

Witham, A. R., Knigge, C., Drew, J. E., et al. 2008, MNRAS, 384, 1277

Wright, N. J., Drake, J. J., Drew, J. E., & Vink, J. S. 2010, ApJ, 713, 871

Yudin, R. V. 2001, A&A, 368, 912

Zorec, J., Frémat, Y., Domiciano de Souza, A., et al. 2016, A&A, 595, A132

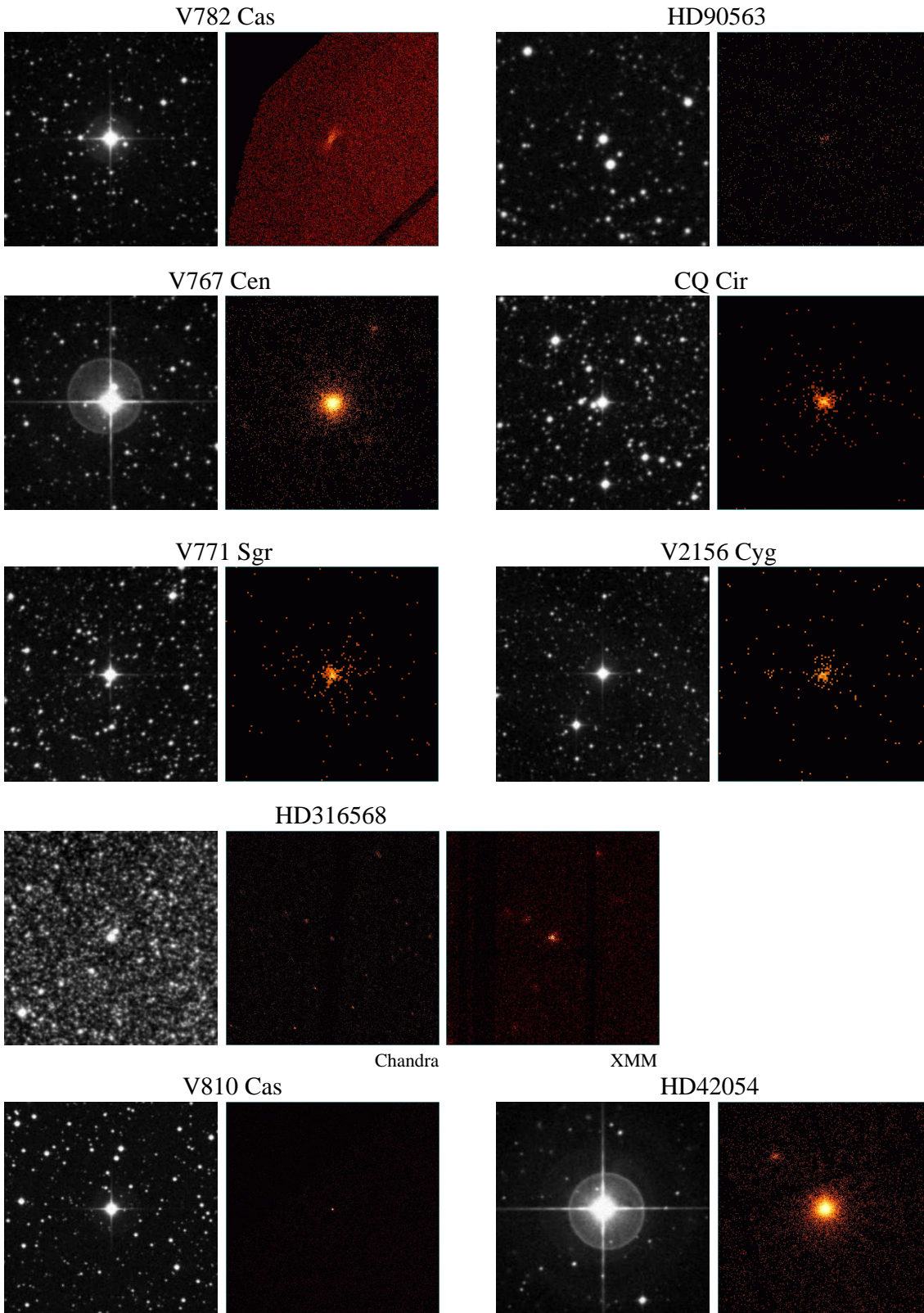V782 Cas

HD90563

V767 Cen

CQ Cir

V771 Sgr

V2156 Cyg

HD316568

Chandra   XMM

V810 Cas

HD42054

Fig. 7. Optical and X-ray images centered on the eight new γ Cas analogs and the γ Cas candidate. All images are centered on the targets, 5'×5' in size, and oriented with north up and east to the left. The X-ray images correspond to the 0.5–10.0 keV energy band (after merging all EPIC data when XMM-*Newton* is used), while the optical images are from the DSS survey (POSS2/UKSTU Red). For HD 316568, the *Chandra* data with ObsID 4547 and the XMM-*Newton* data with ObsID 0402280101 are both shown; for HD 42054, the XMM-*Newton* dataset is shown rather than the zeroth-order *Chandra* data; for CQ Cir, V771 Sgr, and V2156 Cyg, images merging all *Swift* data were created with the online tool (see Sect. 4.2.1).